J. Fluid Mech. (2023), *vol*. 973, A26, doi:10.1017/jfm.2023.519

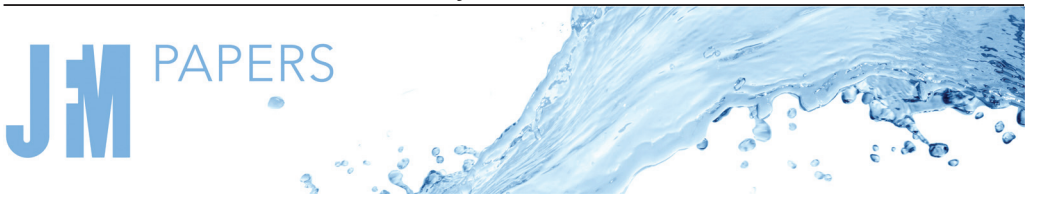

Investigation of shock/shock interferences on the aerodynamics of a fragment in the wake of debris in a rarefied regime/at high altitude

Vincente Cardona[1] **and Viviana Lago**[1],†

[1]ICARE, CNRS, 1C av. de la Recherche Scientifique, CS 50060, F-45071 Orléans cedex 2, France

(Received 24 March 2022; revised 26 April 2023; accepted 12 June 2023)

This work presents an experimental investigation focused on the analysis of aerodynamic properties between two interacting spheres in a supersonic rarefied flow. Atmospheric re-entries of space debris, whether natural or man-made, begin at altitude 120 km, and observations of historical re-entries have shown that fragmentation occurs between 90 and 50 km. The resulting fragments interact with each other, altering their own trajectories while traversing the different flow regimes between the free molecular and continuum regimes. This study focuses on the intermediate slip regime, where viscous effects of varying magnitude can influence the nature of the interactions of the shocks and modify them from the already known behaviour in the continuum regime. Specifically, this study examines how two spheres interact with each other upon re-entry into the atmosphere, focusing particularly on the six types of shock/shock interactions identified by Edney. The experiments were performed in the MARHy wind tunnel, in a steady Mach 4 laminar flow with static pressure 2.67 Pa. To highlight the differences between the six types of interferences, a variety of set-ups and devices were used: flow-field visualization, aerodynamic forces (through two diagnoses, aerodynamic balance and the swinging sphere technique) and wall pressure measurements. Results demonstrate the identification of differences according to the type of interference observed, showing in particular the viscous effect of rarefied flows by making a comparison with the continuum regime.

Key words: aerodynamics, compressible flows, rarefied gas flow

1. State of the art

In 2020, the number of objects launched into space was three times higher than in 2019, due exclusively to commercial activities (ESOC 2021). As the number of objects orbiting the Earth continues to increase, the issue of debris, and consequently debris re-entering the

† Email address for correspondence: viviana.lago@cnrs-orleans.fr

atmosphere, can no longer be dismissed. Moreover, the damage generated by large pieces of debris could be dramatic if the objects reach populated areas (Ailor & Patera 2007). In order to prevent these kinds of negative consequences, various types of studies are being done. Some researchers are developing innovative systems to capture debris before it enters the atmosphere, thereby preserving the active space stations (Flores-Abad *et al.* 2014; More & Murugan 2021). Other studies focus on improving the predictive impact time and area, including estimation of the debris dispersion (Reyhanoglu & Alvarado 2013). Nevertheless, we are still poorly informed about some debris properties, such as the initial state vector, the ambient atmospheric conditions and key parameters, including the ballistic coefficients. The work on the observation of space debris (Hossein *et al.* 2020) has provided information on breakup events (Lips 2003), while fragments from the destruction of space vehicles surviving to the ground have been analysed in order to study how they impacted the Earth (Park & Park 2017), as in the tragic accident of the Colombia shuttle (Ailor *et al.* 2005) or the re-entry of the Chinese space station Tiangong-1 (Ahmad & Fitri 2021). These data may help to build breakup scenarios and improve the predictive capabilities of re-entry debris codes.

Nowadays, atmospheric re-entry trajectory and survivability predictive codes are being developed by research centres and space agencies. The available codes can be classified into two main categories: object-oriented codes and spacecraft-oriented codes Lips & Fritsche (2005). The object-oriented method is based on simplifying the complicated geometry of objects into simple shapes such as sphere, cylinder, box, etc. Tools using this method are DAS, ORSAT and DRAPS. In particular, ORSAT, developed by NASA, also includes thermal/ablation models to determine the debris survivability assessment (Ostrom & Sanchez 2018). The ESA with SCARAB has opted for the spacecraft-oriented method to simulate the re-entry of spacecraft in as real a way as possible; nevertheless, due to a much more complex analysis strategy, this method requires great modelling efforts and computing resources (Lips *et al.* 2004; Koppenwallner *et al.* 2005). PAMPERO developed by the CNES agency since 2013 is another predictive code based on spacecraft-oriented tools (Annaloro *et al.* 2017).

The determination of destructive re-entries and the prediction of the potential for ground risk due to the arrival of fragmented objects on the ground are the main purposes of these numerical codes. The breakup is estimated to occur at altitudes between 90 and 65 km (Kärräng, Lips & Soares 2019) and is the consequence of strong external forces leading generally to the fragmentation of the debris (Prevereaud *et al.* 2012; Lips 2013; Park *et al.* 2020). As a result, one large object becomes a multitude of smaller ones that will interact with each other. These interactions exist at least in the first moments after fragmentation, where the flow is still rarefied. Note that nowadays, this flow regime still needs to be better explored. As evidence, bridging functions describing aero-thermodynamics coefficients, that take into account the different flow regimes involved, are used to improve trajectory predictions and the demise of debris (Park *et al.* 2020). Atmospheric re-entry can lead to different behaviour of the debris' flight depending on its size, shape and material. Evolving at hypersonic velocities, debris entering the atmosphere penetrates an increasingly dense medium as its altitude decreases. Thus it undergoes successively four different flow regimes: free-molecular, transition, slip-flow and continuum. Approaching the Earth, the dynamic pressure and heat flux increase. Most of the time, a small object does not survive this phase, but a larger one can, at least partially, hit the Earth. Different scenarios can occur leading to a longer preservation of the following debris, or to its accelerated destruction. In any case, the interactions between pieces of debris lead to a change in their trajectories, which increases the difficulty of predicting ground impacts (Ahmad

& Fitri 2021). These difficulties are mainly due to viscous effects that have to be taken into account when analysing and describing shock/shock interactions. They concern not only 1 m diameter objects flying at hypersonic speeds, but also smaller parts that are manufactured at high melting temperatures (Koppenwallner, Fritsche & Lips 2001).

Therefore, the topic of proximal bodies is of great interest. The aim of this experimental work is to study how rarefaction and viscous effects could modify the aero-thermodynamic properties of shock/shock interactions. Our motivation is to bring new knowledge to improve the prediction of the fate of objects entering the Earth's atmosphere. This study is not restrictive to this application and can also be useful for other scenarios concerning high speed combined with high altitude of an atmospheric re-entry.

Many studies concerning the interaction of objects focused on the study of Edney's shock/shock interferences (Edney 1968), since they play a major role in the aero-thermodynamics observed behaviours. Numerous experimental and theoretical studies investigated interferences between an oblique shock generated by a wedge and a bow shock, most often produced by a cylinder. These works were motivated by high local heating rates at hypersonic speeds occurring in critical situations, such as shock/shock interferences on a deflected flap, along axial corners in wing–body or on fin–wing junctions. Shock-wave/boundary-layer interactions also occur in air-intakes of breathing propulsive systems. Such interactions can induce separation of the boundary layer, which causes loss in control effectiveness in the engine inlet, with the subsequent reattachment of the separated shear layer giving rise to heat-transfer rates. Many studies have focused on Edney type IV interactions as this is the most critical shock–impact interaction in terms of aero-thermal loads at the wall. Most studies have been carried out experimentally in shock tubes or numerically with a computational fluid dynamics approach, in the continuum regime (Sanderson 1995; Windisch, Reinartz & Müller 2016; Khatta & Gopalan 2018; Paoli 2018). Only a few authors have shown interest in studying the influence of viscous effects on the thermal effects of Edney type IV interactions, and have shown a decrease in heat loads in the slip regime (Carlson & Wilmoth 1992; Glass 1999; Moss *et al.* 1999; Pot *et al.* 1999; Riabov & Botin 1999; Grasso *et al.* 2003; Lu *et al.* 2013).

Regarding the specific subject of space debris re-entry, the geometries of the objects concerned have a closed geometry (spheres, cylinders, cubes, plates) that will form bow shocks. In this context, more recent work has been carried out to study more specifically bow shock interactions, experimentally always in a continuum regime, and numerically in continuum and rarefied regimes (Vashchenkov, Kashkovsky & Ivanov 2003). Some major works investigated interactions between two or several spheres. Indeed, the sphere–sphere case is a canonical geometry that can nevertheless be expected to exhibit many of the important flow features of more realistic geometries. The trajectories of the interacting spheres were analysed experimentally in shock tube facilities using the free flight method (Laurence, Deiterding & Hornung 2007; Laurence, Parziale & Deiterding 2012; Park & Brown 2012; Fisher, Quinn & Smith 2018; Marwege *et al.* 2018; Whalen & Laurence 2021). Only one experimental work concerns the interaction of cylinders in free flight conditions with a hypersonic shock tube (Leiser *et al.* 2022).

The literature shows that studies of the bow shock interaction have so far been conducted in the continuum regime and do not take into account the viscous effects that can occur due to high velocities and low atmospheric density. This experimental work focuses on the study of the interaction between two spheres in a low pressure supersonic flow in the slip regime, representative of an altitude of 76 km. Experiments have been carried out with flow conditions of Mach 4 and ambient pressure 2.67 Pa. Previous work by Cardona, Joussot & Lago (2021) has shown that the different types of Edney interference can be

identified; however, some differences appear with respect to the continuous regime, such as the thickening of the shock and the boundary layer, which leads to the vanishing of the impinging jets that appear in type IV interference. This study goes further and analyses the impact of the viscous effects on the rear sphere in the wake of the first one. In order to simplify this study, it has been chosen to have both spheres of the same diameter. Different diagnostics have been applied in order to analyse the impact of low density on different parameters that influence the aero-thermodynamics of interacting spheres. Shock/shock interferences will be analysed in terms of shock-wave shapes, drag and lift forces, and wall pressure distribution of the second sphere. To complete the study, a pendulum method was adopted to characterize the wake of a sphere in a supersonic rarefied flow. This non-intrusive method will also be used to evaluate the effect of the second sphere on the first one. This experimental work allows the analysis of the influence of viscous effects on the different parameters that are affected by the shock/shock interactions, and of which physical properties are the most affected. In addition, this dataset will allow the validation and improvement of certain physical models, in particular those concerning the aerodynamics used in the debris entry prediction codes. To our knowledge, no experiments have been conducted with two spheres interacting in a rarefied flow. This topic seems to have been exclusively studied experimentally and numerically in a continuum regime, and numerically in a rarefied flow. Still, some parameters are poorly explored, such as the distribution of pressure or heat transfer at the surface of the second sphere. No full study has yet been conducted to link aerodynamic properties with surface parameters such as wall pressure. Numerically, even if calculations representative of rarefied flows are improving, some questions still need to be addressed, in particular, the determination of accommodation coefficients (Zuppardi & Paterna 2015). These parameters originate in slip conditions, thus in the boundary layer of an object. In a rarefied flow, the physics is still poorly understood, which is why some experimental data can provide important information.

2. Experimental conditions

2.1. *MARHy wind tunnel*

The experiments presented in this paper were carried out in the MARHy wind tunnel, one of the three wind tunnels of the FAST platform at ICARE, CNRS (France). MARHy is a rarefied wind tunnel that can create flow from Mach 0.8 up to Mach 20, thanks to the 23 interchangeable nozzles that can generate different low-density flows representative of the early stages of space flight or atmospheric re-entry.

As shown in figure 1, the wind tunnel is composed of three main parts: the settling chamber, the test chamber and the diffuser. The first part is used to establish the stagnation conditions of the flow. The air flow entering the chamber, and hence the static pressure in the settling chamber, are regulated by a gas valve. The air is then accelerated through the chosen nozzle and expands into the test chamber. There, the free-stream conditions depend on the stagnation conditions, the nozzle and the pumping conditions. The third part, the diffuser, links the test chamber to the pumping group, which is composed of two primary type pumps and 14 Roots blowers. The pumping group is able to keep operating conditions in a stable and continuous mode, with no time limit.

Depending on the nozzle used during experiments, the flow can reach a large range of speeds and pressures. For Mach numbers below 5, the test gas is ambient air, which was the case for the set of experiments presented in this paper. For hypersonic flows, the test gas used is dinitrogen. Regardless of the nozzle used, the flow is laminar and continuous

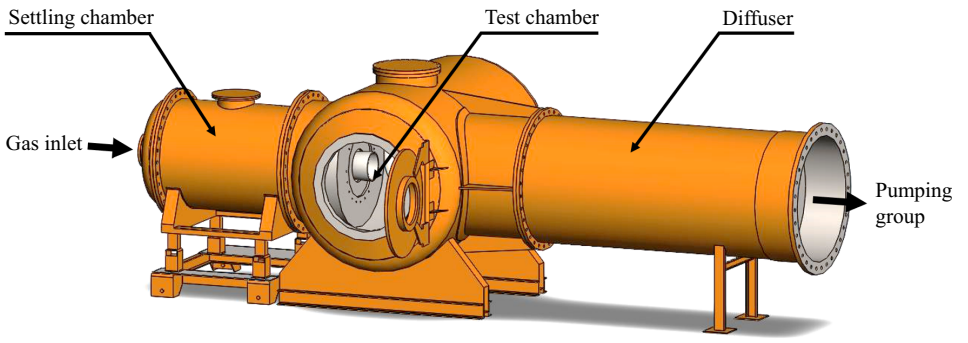

Figure 1. Schematic view of the MARHy wind tunnel.

in the isotropic core thanks to the stable stagnation conditions and the powerful pumping group. The diameter and length of the isotropic core, where the free-stream conditions are well known, depend on the nozzle used.

Stagnation and free-stream conditions are obtained by adjusting, respectively, the pressures in the settling chamber and in the test chamber independently (see figure 1). The stagnation pressure is regulated and stabilized accurately with a micro-valve placed at the inlet of the settling chamber. The free-stream pressure in the test chamber is regulated by commissioning the right number of Roots blowers, and is adjusted by opening the butterfly valve placed between the diffuser and the pumping group. Pressures are monitored with MKS absolute pressure sensors. Their full range is chosen to be in accordance with expected values: a 10 torr sensor for the stagnation pressure (p_o), and 0.1 torr for the free-stream pressure (p_∞), respectively accurate to 0.12 % and 0.15 % of reading. The control of static and infinite upstream flow pressures ensures stable flow conditions in terms of velocity and density. Given the accuracy of the sensors, the maximum Mach number deviation is 2.6 %.

2.2. *Flow conditions*

The purpose of this work was to investigate the interaction of two spherical fragments of debris when re-entering the atmosphere in the upper layers, where the flow regime is rarefied. For the study to be representative of the flow properties of space debris, experimental conditions have to recreate a level of rarefaction equivalent to that at breakup altitude. The rarefaction level is characterized with the mean free path, λ_∞, defined as the distance between two collisions of molecules. Assuming the variable cross-section hard sphere model, this parameter can be calculated with (2.1) (Bird 1994), where ω_∞ is given by the viscosity power law of Sutherland. For the chosen nozzle (Mach 4, 2.67 Pa), whose experimental conditions are presented in table 1, $\omega_\infty = 0.92$ (see Appendix C, table 3) and

$$\lambda_\infty = \frac{\mu_\infty}{\rho_\infty \sqrt{2R_m T_\infty}} \frac{2(7-2\omega_\infty)(5-2\omega_\infty)}{15\sqrt{\pi}}. \tag{2.1}$$

To evaluate the type of flow regime in terms of collisions, very often the free-stream Knudsen number Kn_∞ (see (2.2)) is used to compare the size of the considered object with respect to the mean free path. In the present study the diameter of the first sphere D_1

Stagnation conditions		Free-stream conditions	
Gas	Ambient air	Gas	Ambient air
p_0 (Pa)	404.79	p_∞ (Pa)	2.67
Te_o (K)	293.15	Te_∞ (K)	69.80
ρ_o (kg m^{-3})	4.80×10^{-3}	ρ_∞ (kg m^{-3})	1.33×10^{-4}
		μ_∞ (Pa s)	4.84×10^{-6}
		U_∞ (m s^{-1})	669.92
		Re_∞ (m^{-1})	1.84×10^{4}
		Ma_∞	4.0
		λ_∞ (m)	2.23×10^{-4}

Table 1. Flow conditions of the Mach 4, 2.67 Pa nozzle.

is considered as the reference distance to determine the global Knudsen number:

$$Kn_\infty = \frac{\lambda_\infty}{D_1}. \tag{2.2}$$

Considering an estimated fragmentation altitude between 91 and 50 km, the MSISE-90 model gives a free-stream pressure ranging between 0.1 and 100 Pa, and a mean free path ranging between 3.10^{-2} and 7.10^{-5} m. Ground test experimental simulation of the complete physical conditions of the atmospheric entry of space debris is extremely hard, and there is no facility able to reproduce such conditions. Nevertheless, the study of an analogous rarefaction effect is possible in wind tunnels since another similitude parameter may be used to take into consideration high-speed velocities, namely the similarity number (Chambre & Schaaf 1961; Wuest 1974; Macrossan 2007), described with

$$\varsigma = \frac{Ma_\infty}{\sqrt{Re_\infty}}. \tag{2.3}$$

As can be seen, this parameter is based on the appropriate Mach and Reynolds numbers, taking into account dynamic and viscosity effects. As discussed in Cardona *et al.* (2021), the chosen models (see § 2.3) and nozzle give $\varsigma = 0.233$ and $Kn_\infty = 0.0139$. When considering the similarity parameter, experimental conditions are representative of a 1 m diameter main debris fragmenting at 76 km in altitude, according to the MSISE-90 atmospheric model and the velocities given in Prevereaud *et al.* (2012). Consequently, free-stream experimental conditions are coherent with the expected level of rarefaction at fragmentation altitudes.

2.3. *Models and general configuration of the set-up*

The experiments presented in this paper were carried out in the MARHy wind tunnel described above, equipped with the nozzle detailed in table 1.

Two spheres were used as experimental models that act as blunt bodies that represent a large variety of debris shapes. The first sphere, S_1, represents the parent debris, and the second sphere, S_2, a debris fragment detached from S_1. The spheres are made of Polyoxymethylene (POM), painted with thin black spray paint to increase contrast and improve image analysis. Painted, they both have same size (16 mm diameter) and mass (2.88 g with the paint). The choice of the diameter of the spheres was motivated by

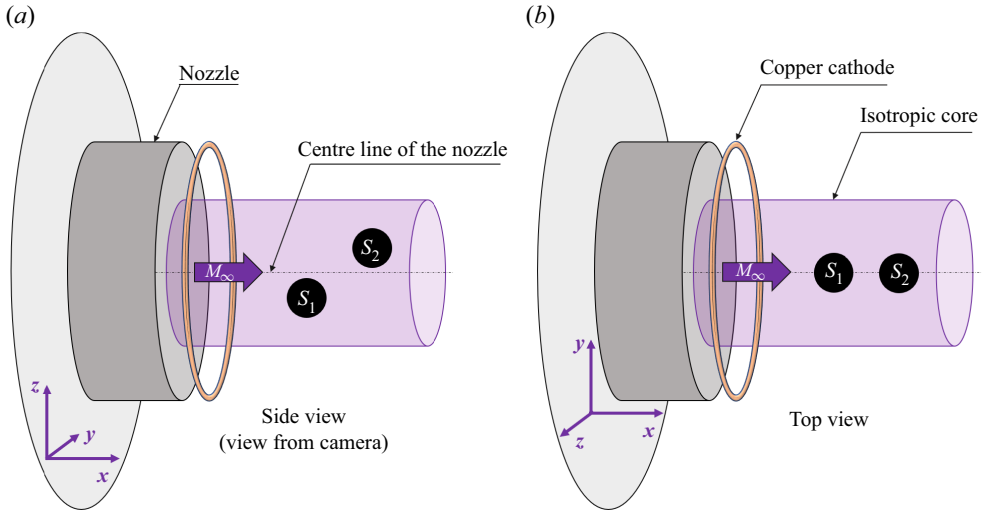

Figure 2. General configuration of the set-up.

different reasons: the spheres must be large enough to be instrumented and also to allow an accurate visualization of the flow around them; but at the same time, they must not be too large to ensure that the shock of the two spheres can always be contained in the useful core of the flow whatever the relative position of the two spheres.

As described schematically in figure 2, the axes of symmetry of the two spheres are aligned with the vertical plane $Y = 0$ passing through the axis of symmetry of the nozzle. The experiment consists in moving the second sphere vertically, leaving the first one fixed, in order to analyse the physical properties of the interaction of the shocks produced by the two spheres. The outside diameter of the divergent nozzle is 220 mm, but the isentropic flow core is only 75 mm in diameter. In order to have enough clearance to move sphere S_2, the centre of S_1 is placed at $Z = -30$ mm. As presented in Cardona *et al.* (2021), this position does not significantly alter the free-stream flow seen by S_1, or its shock-wave shape. Moreover, since the point of interest is the effect of shock/shock interferences, if S_1 is always at the same position in the flow, then even a slight modification in its shock waves will not impact our study much. The second sphere will be moved to many different positions behind S_1 in the $\boldsymbol{x}$ and $\boldsymbol{z}$ axes. Throughout this work, the stagnation point of S_1 is taken as the origin of the spatial reference, and the axes $\boldsymbol{x}$, $\boldsymbol{y}$ and $\boldsymbol{z}$ are oriented as shown in figure 2. Here, (X_2, Z_2) are the coordinates of the nose of S_2 in this spatial reference. More details concerning the different set-ups will be given in § 3.

3. Experimental devices and post-processing

3.1. *Flow-field visualization*

3.1.1. *Set-up*

To visualize the flow field, the two spheres are held in position with profiled supports, which do not obstruct the flow. Sphere S_1 is maintained with a vertical support fixed in a rotary system to allow the sphere to be removed from the flow in order to record background images. Sphere S_2 is maintained with a horizontal support coming from the rear of the sphere so as not to be intrusive. This support is fixed on a triaxial displacement

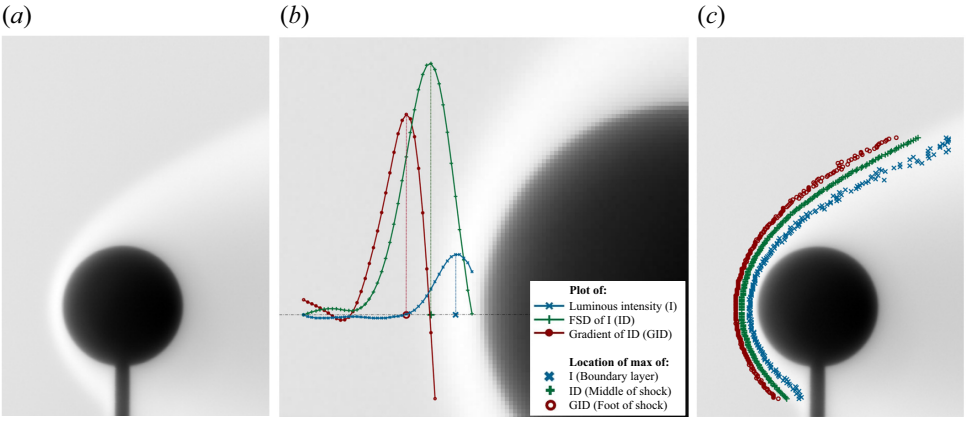

Figure 3. Detection of a sphere thick shock wave. (*a*) Normalised image of the flow around a single sphere; (*b*) detection method on a pixel line; (*c*) result of shock-wave detection on the entire image.

system so that S_2 can be moved in the wake of S_1, and also removed from the flow for the recording of background images.

The low density of current experimental conditions does not allow the application of common techniques such as schlieren or particle image velocimetry to visualize and analyse the flow field. A technique used less commonly but adapted to our experimental conditions is used in this work. It is the technique of the glow discharge based on a cathode to ionize molecules. In our experiment, the cathode was made of copper and was placed upstream of the models around the exit of the nozzle, as shown in figure 2. It consists in applying an electrical discharge on a cathode placed near the flow. A negative voltage $-1\,\mathrm{kV}$ is applied on the copper ring, inducing current $4\,\mathrm{mA}$. The polarization is low enough not to modify the nature of the flow (Coumar & Lago 2017). With this method, a local increase in density induces an increase in the local emitted luminous intensity. Since a shock wave is a compression of molecules, the glow discharge makes it possible to determine visually the shock waves of the spheres, by analysing the brighter region.

This method generates a volumetric illumination of the flow. Consequently, all the images taken are the result of luminous integration in the line of sight of the eye or of any recording tool. So even if the glow discharge technique can determine shock waves, the local density cannot be calculated with a simple scaling law.

Images were recorded with a Kuro CMOS camera using back illumination. The camera is equipped with a VUV objective lens that gives a resolution $154\,\mu\mathrm{m\,px^{-1}}$. For each relative positioning of the spheres (S_1 and S_2 fixed during acquisition), a set of 200 raw images was recorded, with exposure time 60 ms. An equivalent set of images without the models in the flow was recorded as background image. For each position, images of the flow are averaged and divided by the mean background image. This processing allows us to reduce the noise of images and avoid luminous gradient due to the experimental set-up. The resulting normalized image, shown in figure 3(*a*), presents an improved luminous contrast of images that allows the analysis of shock waves.

3.1.2. *Shock-wave detection*

Images give important information, in particular, on shock-wave shapes. In our study, the detection of shock waves is a key step to determine the type of shock/shock interferences

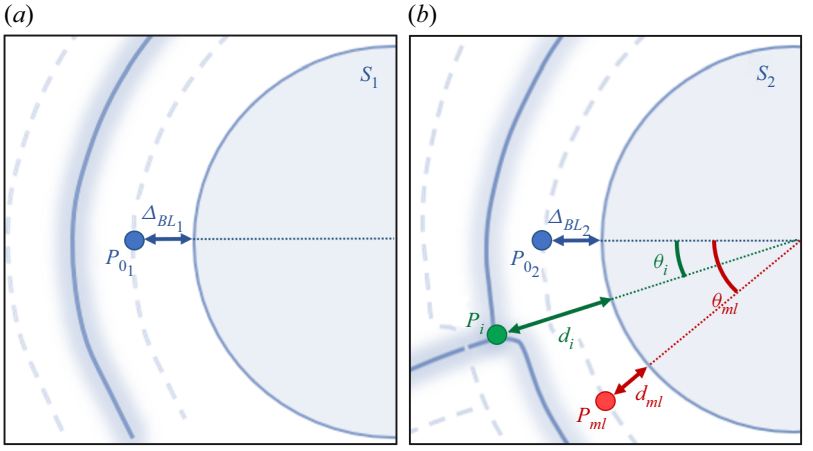

Figure 4. Detection of points of interest: intersection point between S_1 and S_2 middle shock (P_i), point of maximum luminosity in the intersection area (P_{ml}), and points of maximum luminosity along the stagnation line of S_1 and S_2 (P_{0_1} and P_{0_2}).

that occur. This detection is based on the luminous intensity of the images. Kovacs *et al.* (2022) proposed the Fourier self-deconvolution (FSD) method, which was developed and validated for our specific experimental conditions. This method is applied to the present work. As illustrated in figure 3(*b*), the luminous intensity in analysed for each horizontal line of pixels, and allows us to define three regions due to the thickness of the shock wave: the maximal intensity, the FSD maximum, and the maximum of the FSD derivative. In what follows, the three regions will be named, from upstream to the surface of the sphere, as: foot of shock (FS), middle of shock (MS), and boundary layer (BL). Concerning this last region, the maximum luminosity is representative of the denser region. Close to the surface of the sphere, particularly at the front half, this denser region corresponds to the boundary layer. Outside this area, this term of BL is inappropriate. However, it will be more convenient to call it BL in the rest of this paper. Note that the region between the FS and the BL is called 'middle' but obviously, it is not located at the centre. Applying the method on each horizontal line of pixels of the image, we obtain three well-plotted regions corresponding to the regions described previously, as shown in figure 3(*c*).

The analysis of the images, and more specifically the intensity values, can also provide important information to locate regions of stronger interactions. Figure 4 shows the four main points that will be used to deepen the knowledge on the effect of shock/shock interferences in supersonic rarefied flows. Thanks to the shock-wave detection, the intersection point P_i between the middle shock of the two spheres is found, where P_i is characterized by d_i and Θ_i. Throughout this work, Θ_i will be used as the reference parameter to reflect the relative positions of the spheres. Concerning the other three points of interest, their locations are based on the luminous intensity of the image. By finding the point of maximum luminosity in the intersection area, P_{ml}, the maximum local density can be found. The last two points, P_{0_1} and P_{0_2}, concern the maximum luminosity on the horizontal line passing by the nose of the spheres. Here, Δ_{BL_1} and Δ_{BL_2}, respectively, give the boundary layer stand-off distances of S_1 and S_2. In addition to location information, these three points contain intensity values that make it possible to compare the level of density of each type of shock/shock interference. All the data from P_{0_1} will serve as normalizing parameters.

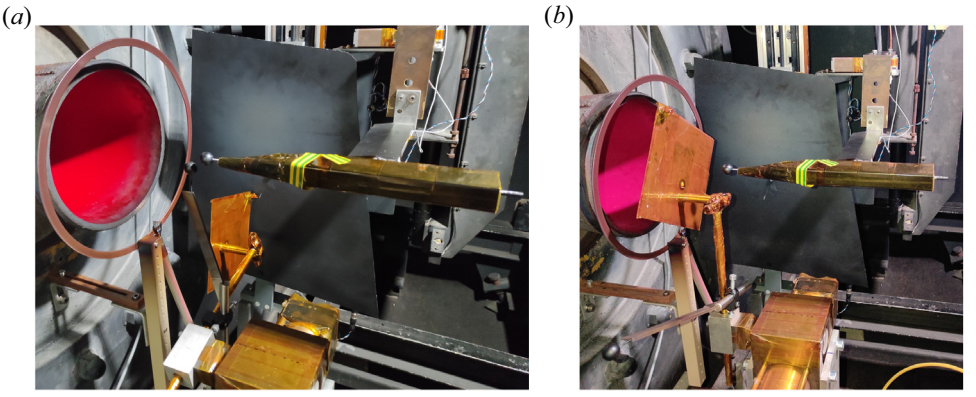

Figure 5. Forces balance set-up. Pictures of a measurement of (*a*) the total forces, and (*b*) the residual forces.

3.2. *Drag and lift force measurements*

The aerodynamic forces of the spheres for the different interference cases studied were measured. Force measurements were carried out with two different methods. The simplest device is a pendulum balance method that consists in suspending a sphere with wires to measure drag forces from the angle deviation. The second method is the use of an aerodynamic balance to measure drag and lift forces. The two methods are complementary, and the results obtained with these two devices will be compared.

3.2.1. *Aerodynamic balance*

The aerodynamic balance used in this investigation was designed and experimented by Noubel & Lago (2021). It was developed especially for low-density flow conditions, such as those in the MARHy wind tunnel, where the force values are estimated to be between 1 mN and 1 N. The balance is a sting type and comprises two modules to measure drag and lift forces.

The drag and lift forces are required for the following sphere (S_2). It is thus screwed until its centre of gravity on the sting of the aerodynamic balance. The balance is positioned horizontally in the flow and fixed to a triaxial displacement system as presented in figure 5.

The balance is positioned horizontally to avoid gravity effects, as explained by Noubel & Lago (2021). Thus lift forces are measured in the y-direction, so the second sphere will be displaced in the y-direction and not in the z-direction as for the other experiments. Since the flow in the core is isotropic, the change in direction does not modify the physics of the shock/shock interferences or the physical values. The positioning is controlled with a camera placed on top of the test chamber.

Sphere S_1 and a plate are placed in a rotary system so that the sphere is in either the flow (figure 5*a*) or the plate (figure 5*b*). The usefulness of this system will be explained in the next paragraph. The first sphere is placed as described in § 3.1 (figure 5*a*), but this time, to keep the same displacement area for the second sphere, S_1 off-centre from the middle of the nozzle is in the y-direction ($Z = 0$ mm, $Y = -30$ mm).

For each position of S_2, two measures have to be realized: with S_1 in the flow (figure 5*a*), and with a plate hiding S_2 from the flow (figure 5*b*). The first measurement records the total drag and lift forces, including residual forces induced by the suction of the pumping group, or vibration from the pumping group. The second measurement records only the residual forces. The acquisition time, both with and without the plate, is 10 s, with acquisition

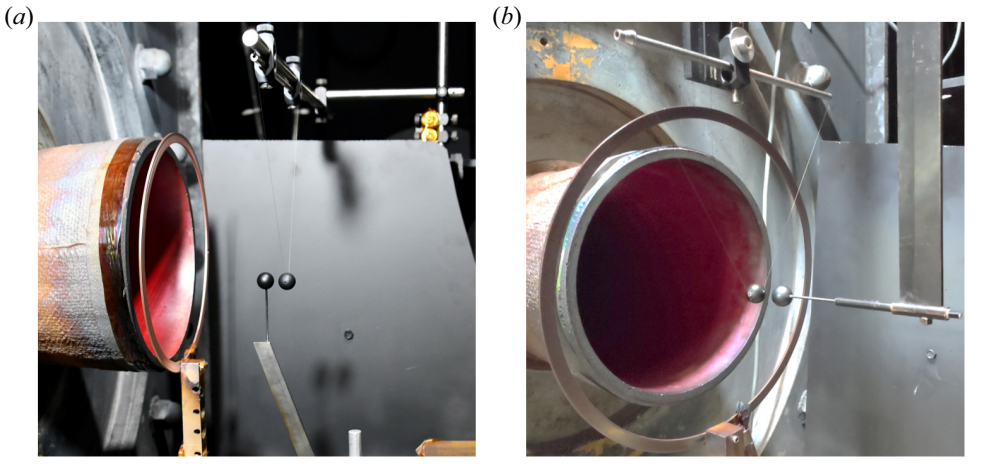

Figure 6. Picture of the swinging sphere experiments: (*a*) method applied on S_2 supported by a moving support; (*b*) method applied with S_1 supported by a fixed support, and S_2 moving.

frequency 1000 kHz. These two steps are repeated five times. For each module, drag and lift, values are averaged and the residual force values are subtracted from the total force to obtain the real drag and lift forces.

3.2.2. *Swinging sphere method*

This method consists in suspending the second sphere by a wire system so that it can move freely according to the surrounding flow. The angle of deviation of the sphere will depend on the force acting on the sphere, the measurement of which allows the aerodynamic force to be deduced (Cardona & Lago 2022). As shown in figure 6, the swinging sphere method was employed in two different ways. In figure 6(*a*), the suspended sphere is the second one, in order to measure the impact of S_1 over S_2. In figure 6(*b*), on the contrary, the first sphere is suspended, in order to measure the effect of S_2 on S_1.

In both cases, the suspended sphere is drilled from side to side on an axis passing through its centre. A thin, inelastic wire of 0.07 mm diameter passes through the hole in the sphere and through the hole in a hollow tube that serves as a support to hold it like a swing. This tube is positioned horizontally, parallel to the y–z plane so as to give a single degree of freedom along the x axis. In order to avoid any movement in the $\boldsymbol{y}$-direction, the wire is glued to the sphere and to the stem. To obtain precise results, the sphere is positioned so that both sides of the wire have the same length, forming an isosceles triangle with the straight stem as base. This experiment is analysed from images obtained with the Kuro camera equipped with the VUV lens described in § 3.1. Despite the high stability of the flow and the equilibrium state reached by S_2, a slight movement of very small amplitude may affect the sphere. To improve the quality image definition, the images were recorded with very short acquisition times since the aim is to detect accurately moving spheres and wires. On the contrary, due to the size of each image, the duration of acquisition must not be too long so that the sets of images generated are not heavy files. A good compromise was to set the acquisition time to 20 ms per image.

For the experiment that consists in studying the movement of the sphere S_2 (figure 6*a*), S_1 is set as for the set-up of flow visualization described in § 3.1. The tube that holds the wires of S_2 is attached to a triaxial Cartesian displacement system, which aligns S_2

with S_1 in the same vertical plane that passes through $Y = 0$. After the flow has been established and stabilized, S_2 is first placed in its initial position, right behind S_1 in the $\boldsymbol{x}$-direction. The experiment then consists in moving the tube vertically, or horizontally with the displacement system with constant speed $0.8\,\mathrm{mm\,s^{-1}}$. As S_2 is moved in the wake of S_1, the sphere progressively balances itself so that it compensates for the forces induced by the flow.

For the second experiment (figure 6*b*), S_1 is suspended by the swinging system. The holding tube of S_1 is then fixed to the wall of the test chamber. The second sphere is held by the same moving system as the one described in § 3.1. Both spheres are placed in the same positions as described in § 2.3. In this experiment, the support of S_1 does not move, and only S_1 responds to the experienced forces. This time, it is S_2 that is displaced behind S_1 to study the impact of its positioning on the upstream sphere. For this experiment, some positions of S_2 were studied. Images were recorded with stationary positions for reasons that are explained in Appendix A.

The determination of the force value of the suspended sphere is based on the measurement of the angle of its wires with respect to the vertical, as detailed in Cardona & Lago (2022). Assuming an equilibrium state of the sphere in each image (i.e. acceleration $0\,\mathrm{m\,s^{-2}}$ is considered), Cardona & Lago (2022) demonstrated that the drag force F_x of the sphere is given by

$$F_x = m\,g\,\sin(\alpha). \tag{3.1}$$

With the manual detection of the wire, and automatic detection of the sphere, accuracy ± 1 px for both the centre of the sphere and the wire is assumed. Consequently, the real angle is given with estimated accuracy $\pm 0.4^\circ$, and the drag force of each position with accuracy ± 0.18 mN. This method was validated by comparing the drag forces of a single sphere obtained by Cardona & Lago (2022) and literature results. In the present work, the swinging method is applied to an interactive sphere (S_2) to study the effects of interaction. Results are compared to those obtained with the aerodynamic balance in the same experimental conditions in Appendix B. These two methods show a good agreement, which allows us to be confident with the results obtained with the swinging method.

3.3. *Surface pressure measurement*

The set-up used for the measurement of wall pressure of the second sphere S_2 is shown in figure 7. The purpose is to measure the pressure at the surface of the second sphere in the meridian plane for every interference type investigated. The assembly of the first sphere remains unchanged from that described in § 3.1. The second sphere is drilled as shown in the top sectional view of figure 7. A hole of 1.2 mm diameter along a radius of S_2 is made to measure wall pressure. This diameter is chosen according to two experimental constraints. The hole must be small enough to have a highly localized measurement of the pressure at the surface of S_2. At the same time, as the pressures at the surface of the sphere are very low, the diameter of the hole must be large enough to reach equilibrium with the pressure sensor, to which the pressure line is linked, in a reasonable time. A second larger hole is made perpendicular to the first, into which a stainless steel tube is inserted. This tube is used to hold the sphere in position and to connect the wall pressure measurement hole to the pressure sensor. This tube is placed on a horizontal plane and perpendicular to the flow axis. Its diameter was chosen according to two parameters: not to obstruct the flow too much, but to hold the sphere sufficiently so that it does not vibrate with the forces exerted by the flow. At the opposite end of the sphere, the tube is maintained in a precision rotating system. As can be seen on the scheme, in the side view of figure 7,

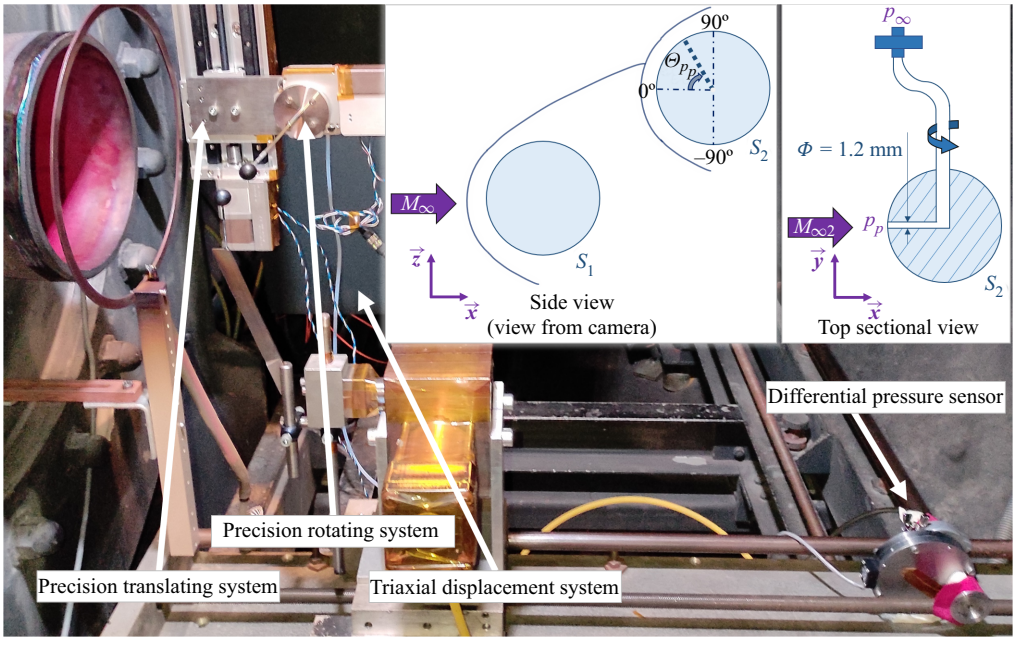

Figure 7. Picture and schematics of the surface pressure measurement.

this rotating system can rotate S_2 without moving it towards S_1. Therefore, the hole of S_2 moves along the perimeter of the vertical plane at its surface, allowing wall pressure measurements at different angles. The rotating system is in turn supported by a precision vertical translation system enabling the precise movement of S_2 to obtain the six types of shock/shock interference. The whole assembly is held on the triaxial displacement system. The wall pressure is measured with a pressure sensor that is placed inside the experimental chamber, out of the flow. This minimizes the distance between the measuring point and the sensor; the pressure line is connected by a flexible tube. The sensor is placed vertically on a support that absorbs vibrations, so that the membrane separating two identical pressure cavities does not undergo gravity or vibrations. The sensor is a Validyne DP103 that measures the differential pressure between the surface hole and the residual pressure in the test chamber p_∞. The sensor measures very low pressures up to 0.0125 psi, i.e. 86 Pa, and is accurate at 0.5 % of the full scale, i.e. 0.43 Pa.

For each position of S_2, thus for each interference case studied, the wall pressure of S_2 was measured over an angular section ranging between 90° and −90°, as described in the side view in figure 7. For each angle, it is necessary to wait as long as needed to stabilize the pressure. For each position of S_2, once the pressure has been measured for all angles, the sphere is rotated to its initial angle, and a new measurement is realized to ensure that there is no deviation in values during the time of the experiment (∼4 h).

4. Shock/shock interference analysis for a fixed longitudinal distance

4.1. *Identifications of the type of shock/shock interference*

In a first study (Cardona *et al.* 2021), numerous images were recorded for a large set of positions, varying both X_2 and Z_2. As investigated in the continuum regime (Edney 1968), six different patterns were identified. Even though the results gave first knowledge of

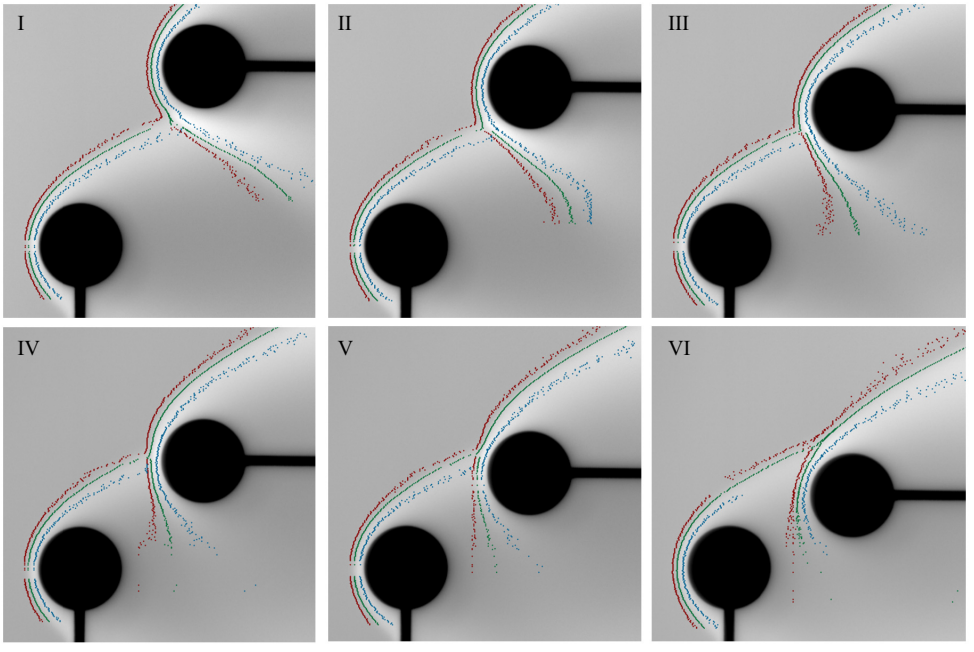

Figure 8. Images of the SSIs and their detected shock waves (red indicates FS, green indicates MS, blue indicates BL).

shock/shock interferences (SSIs) in a supersonic rarefied flow, the mapping of the positions of S_2 described in this previous work was not ideal. Indeed, the position grid was not fine enough. Moreover, the results were obtained for different X_2 positions, which induces a variation of the pressure perceived by S_2 along the shock of S_1. And when one moves away longitudinally from S_1, the structure of the shock of S_1 is modified because the pressure in the shock changes; it becomes more diffuse, which also affects the flow field in the wake of S_1. Therefore, the interaction of the shocks of S_1 and S_2 is also modified as a function of the position X_2. In addition to these effects, the angle of incidence of the shock from S_1 on S_2 is also changed when S_2 moves away longitudinally from S_1. All of these variations would not allow the SSI effects to be decoupled from these flow variations. However, the purpose of the present study is to evaluate the specifics of each type of interference in a rarefied flow. We therefore chose to fix the longitudinal position of X_2 of the second sphere and move it only in the vertical direction, keeping the angle of the incident shock constant. It was chosen to place the nose of S_2 24 mm behind that of S_1 in the x-direction, resulting in incident shock angle 25°. As the second sphere moves down in the wake of the first one, its shock wave intersects the shock wave of S_1, in six different ways. Figure 8 shows the images obtained for the six types of interference first described by Cardona *et al.* (2021), and detailed more accurately in the present work.

In order to analyse SSIs qualitatively, the S_1 and S_2 shock waves were superposed as shown in figure 9.

Many relative positions of S_2 with respect to S_1 ($X_2/r_1 = 3$, with r_1 the radius of S_1) other than those given in figures 8 and 9 were recorded. This made it possible to classify the SSIs in terms of coordinates and thus of intersection angles Θ_i, as shown in figure 10. Since shock waves are thick and diffused in rarefied flows, the SSI characteristics are not as clearly defined as in the continuum regime, where pressures are higher. This means that

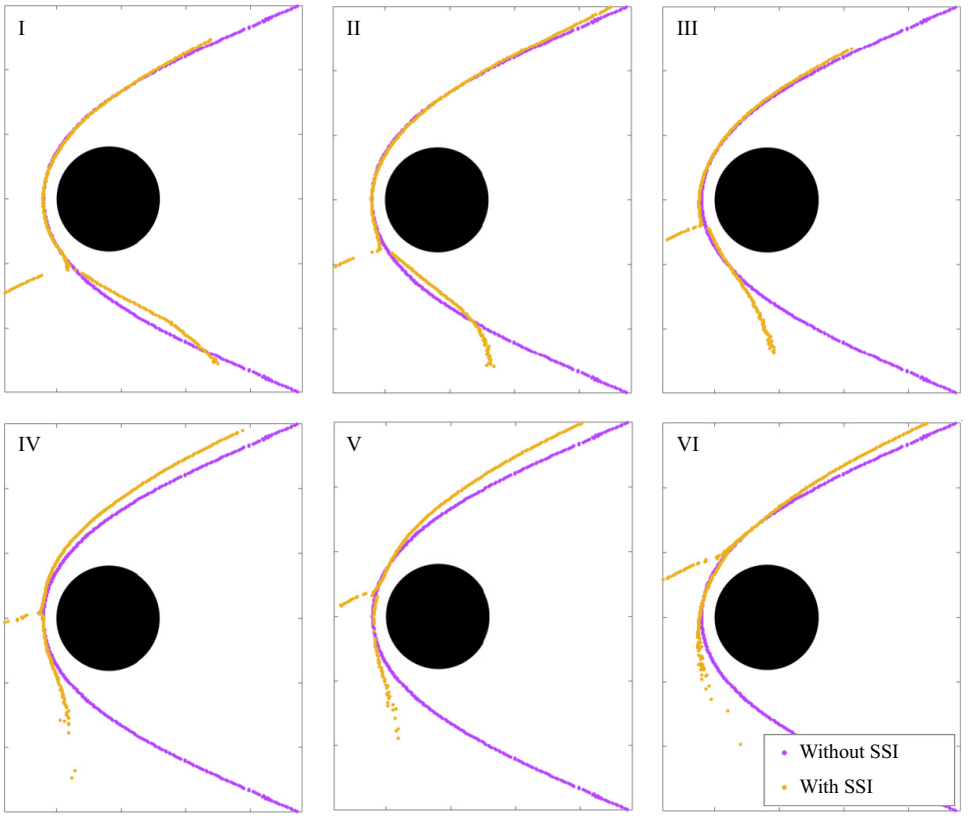

Figure 9. Superposition of S_1 (reference case without interference) and S_2 (with interference) middle shock waves for each type of interference.

transitions between two types of SSI are smooth and are given as a function of the angle area. Consequently, the determined angles described in figure 10 delineate transition areas.

A detailed qualitative analysis of figures 9 and 8 reveals several important features.

(i) Considering the sphere S_2, its shock is not symmetrical, unlike for S_1. The lower flow region is affected by the presence of the first sphere, and particularly the flow conditions that it creates.

(ii) For all types of interference, from I to VI, we see that the shock angle of the lower part of the S_2 shock wave increases. For types I and II, below the intersection point, the S_2 shock wave is pushed by the incident shock. Then, as S_2 descends, it enters the wake of S_1, where the level of rarefaction increases as the local pressure decreases. Hence the lower part of the S_2 shock wave is less compressed: it expands and gets thicker.

(iii) For types IV, V and VI SSIs, the incident shock wave, coming from S_1, interferes with the upper part of the S_2 shock wave ($\Theta_i > -5^\circ$). For type IV, the S_1 and S_2 shock waves intersect almost perpendicularly, while for types V and VI, the two shocks go in the same direction (north-east). Either way, one part of the molecules arriving with the S_1 shock wave penetrates under the upper part of the S_2 shock wave. Consequently, the S_2 shock wave deviates upwards. For type VI, this effect

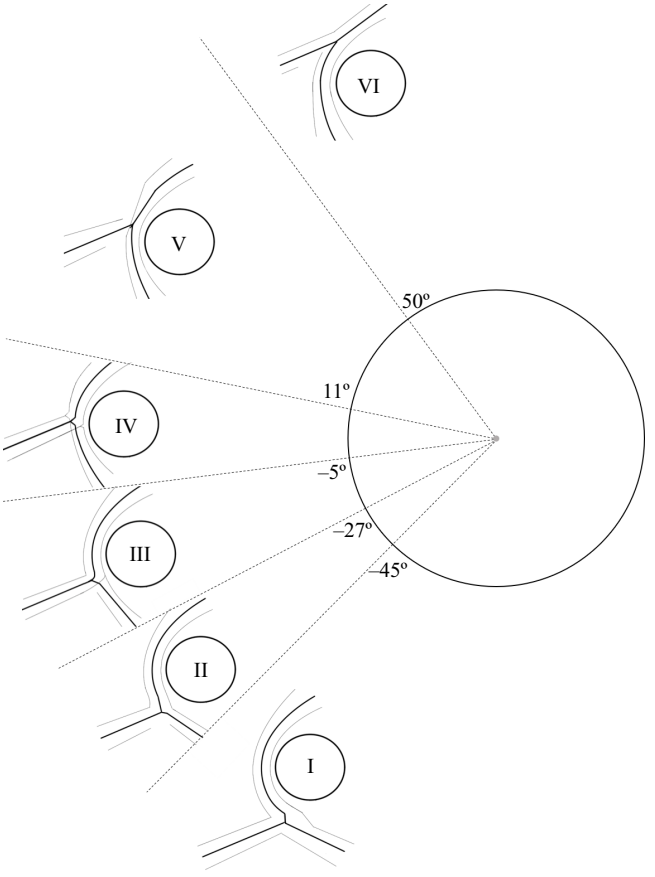

Figure 10. Schematics of SSIs with the associated range of incident shock angle.

diminishes due to the fact that as S_2 goes down in the wake of S_1, the S_1 shock wave will progressively go above the shock wave of S_2 until there is no SSI.

(iv) From type I to type III, below the point of intersection ($\Theta < \Theta_i$), the curvature of the S_2 shock wave appears to flatten, while for types V and VI, the flattening occurs above the point of intersection ($\Theta > \Theta_i$). This behaviour is probably related to the location of the pressure peaks deforming the shock wave of the second sphere.

(v) Another peculiarity of the type I–IV patterns is the presence of a recoil zone, where the point of intersection of the shocks appears to be pushed farther ahead of S_2. This seems to occur when the shock waves from S_1 and S_2 meet with different orientations, one going north-east and the other south-east. Moreover, this feature is not observable for types V and VI, where the shock waves follow the same direction (north-east).

In the following, the six interference types that have been identified will be investigated in terms of visualization, aerodynamic forces and wall pressure measurements.

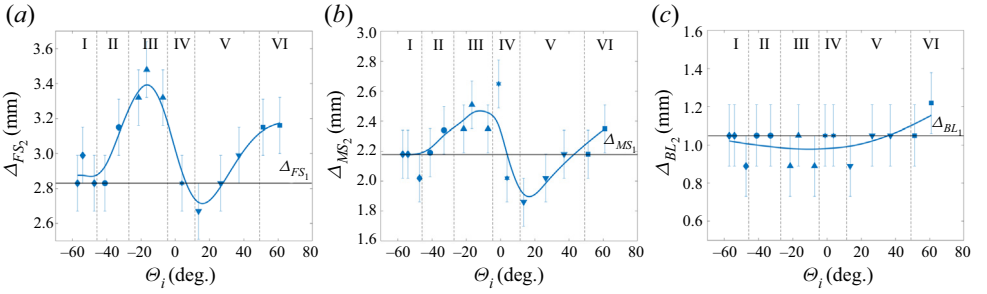

Figure 11. Shock stand-off distances of S_2 according to the type of interference: (*a*) foot shock, (*b*) middle shock, and (*c*) boundary layer.

4.2. *Identification of points of interest and their characteristics*

4.2.1. *Stand-off distances*

The shock-wave detection method allowed us to identify three regions of shock. On the horizontal line from the nose of the sphere (see the horizontal lines in the two schemes in figure 4), the stand-off distances (Δ) of the foot shock (FS), middle shock (MS) and boundary layer (BL) were determined. Figure 11 presents the evolution of these stand-off distances as a function of the angle of intersection Θ_i, and reveals the deformation of the shock waves on the horizontal line of S_2. These results were not observed in Cardona *et al.* (2021) where X_2, and thus the incident shock angle, varied, suggesting that the incident shock angle tends to influence the SSI, as has been found in many other studies in the continuous regime (Edney 1968; Keyes & Hains 1973; Borovoy *et al.* 1997; Boldyrev *et al.* 2001; Peng *et al.* 2020). Nevertheless, to investigate the influence of the incident shock angle under rarefied conditions, further study would be required. On the three graphs in figure 11, the black lines represent the mean value for stand-off distances of S_1, which do not change (with ± 0.154 mm accuracy) whatever the vertical position (Z_2-coordinate) of S_2. Since S_2 has exactly the same diameter as S_1, Δ_1 also represents the stand-off distances that S_2 should have without any interactions.

As observed, the stand-off distances for the sphere S_2 (Δ_2) are strongly impacted. Note that Δ_{BL_2} is almost constant (figure 11*c*), except for type VI SSIs, where an increase can be observed. It corresponds to positions where S_2 enters the wake of S_1 more deeply, i.e. where the local mean free path also increases. This is in agreement with Rembaut, Joussot & Lago (2020) and Akhlaghi & Roohi (2021) who showed that an increase in the rarefaction level leads to an increase in Δ, and therefore to an increase in Δ_2 for type VI SSIs.

For all the five other types of interference, the analysis is based on Δ_{FS_2} and Δ_{MS_2}. For type I SSIs, the stagnation line of S_2 is not impacted. The area of interaction affects only a small area of the lower part of the shock. Then, from type II to type III, Δ_2 increases strongly. From a detailed analysis of the schematics of SSI in figure 10, it seems that the shock wave of S_1 penetrates in between the surface of S_2 and its shock wave by going up, pushing it away at the nose. The range of angles of type IV SSIs seems to be a transitional area, where the stand-off distances suddenly decrease. This could be due to the particular impact where the two shock waves meet almost perpendicularly around the nose of S_2. This creates a V-shaped deformation of the shock, which seems pushed away from S_2 surface above its nose. But at the nose, the strong incident shock wave penetrates deeper into the shock wave of S_2, decreasing the stand-off distances of both its FS and MS. Types V and

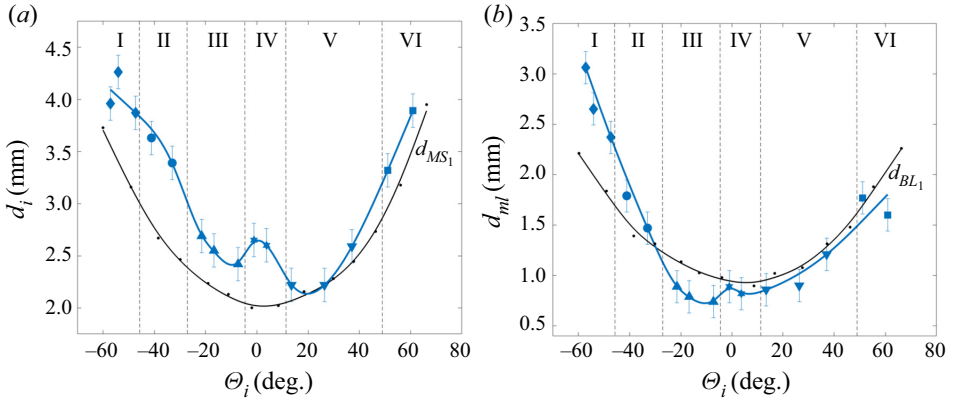

Figure 12. Distances of (*a*) the interaction point and (*b*) the most luminous point in the shock/shock interaction area from the surface of the sphere, according to the type of interference.

VI SSIs do not impact the shock wave shape much at the stagnation point. As discussed above, the increase in Δ is due mostly to the increase in rarefaction level.

4.2.2. *Distances between the interaction area and the surface of S_2*

Figure 12 shows the points of interest P_i and P_{ml} that we identified in figure 4. Distances d_i and d_{ml} were determined on the S_2 shock wave for each angle of intersection Θ_i. Here, P_i is located at the intersection between the middle of the shock waves so it refers to the middle shock region, and P_{ml} is the most luminous point in the intersection area so it refers to the boundary layer region. Thus d_i and d_{ml} are, respectively, compared to d_{MS_1} and to d_{BL_1}, the distances of the shock wave without SSI.

First, it is important to note that d_i remains greater than or equal to its reference value (d_{MS_1}), while this is not the case for d_{ml} as it is smaller than its reference value (d_{BL_1}) from types III to VI SSI. This means that in the intersection area, the middle of the shock is mostly pushed away from the surface of S_2, while the boundary layer is mostly pushed towards it. Consequently, in this area, shock waves are thicker and more diffuse, increasing the viscous effect at the wall of the sphere.

Also, another remarkable feature of the curves in figure 12 is the V-shape that appears around the interference angle 0°. This area shows a very localized increase in the stand-off distance for both the shock interaction and the point of greatest brightness that reflects the point of greatest density. This feature can also be observed in the specific shape of the type IV SSI shown in figure 10 in a schematic way, and in the image in figure 8. Curiously, it is more marked than any other aspects of SSI shapes. This is consistent with the fact that the type IV SSI is a transition region where the interaction of shocks exhibits compression, as can be seen in figure 11, where the distances of the different shock regions become smaller than the reference distances.

4.2.3. *Intensity levels in the intersection area*

Another interesting observation that deserves analysis is the distribution of the light intensity in the area of the shock interaction. Even if the intensity is not exactly proportional to the density, it gives information concerning the impact of SSI on the local density. In figure 13, the intensity level of P_{ml} (I_{ml} in figure 13*a*) and of the most luminous

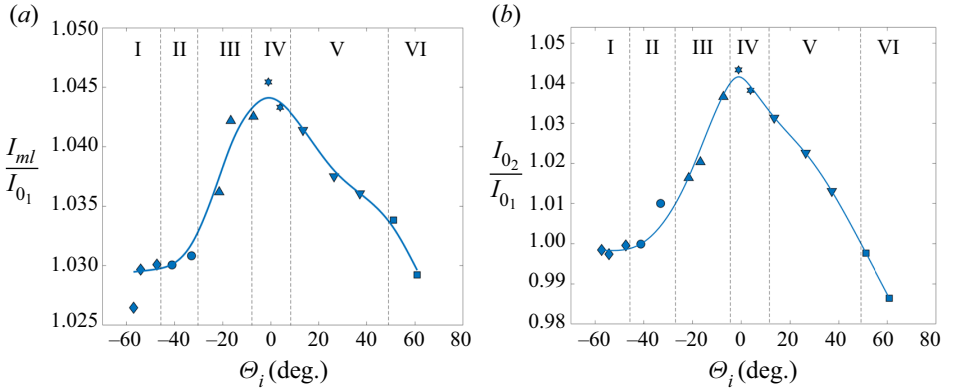

Figure 13. Intensity values of the most luminous points (*a*) in the shock/shock interaction area, and (*b*) on the stagnation line, according to the type of interference.

point passing by the nose of S_2 (I_{0_2} in figure 13*b*) are plotted. In order to compare the intensity levels of the different images, their values have been normalized with I_{0_1} of each image. It should be noted that I_{0_1}, located at the stagnation line of S_1, is the densest point of a single sphere, and its value is the one that S_2 should have without any interaction.

As shown in figure 13, the two tendencies are the same: the slopes increase from type I to IV, and then decrease from type IV to VI. Figure 13(*b*) shows the light intensity at the S_2 stagnation point normalized to that of S_1. The curve shows a maximum for the type IV SSI, which is representative, for this type of interaction, of an increase in local density in front of S_2. Figure 13(*a*) presents the evolution of I_{ml}, showing that whatever the type of SSI, the local density in the intersection zone of the shocks is higher than the maximum density observed at the stagnation point of the S_1 sphere taken as reference. On the other hand, the graph in figure 13(*b*) shows for type I, where the sphere is almost out of the influence of the shock wave S_1, that the densities of the two stagnation points are equal. This is consistent, since the free flows seen by S_1 and S_2 are the same. Then, from type II to type VI, the intensity values vary in the same way as for P_{ml}. Approaching type VI, the density at P_{0_2} becomes lower than that at P_{0_1}, leading to an increase in separation distances due to a higher level of rarefaction. Also, the mean free path increases, and the free flux density decreases as well as the local density in the shock wave of S_2.

4.3. *Drag and lift*

4.3.1. *Drag and lift analysis*

The aerodynamic balance described in § 3.2 was used to measure the drag and lift forces of S_1 alone, and of S_2 interacting with S_1. From the previous images, the six relative positions of the sphere were selected to observe the impact of the different SSI on the aerodynamic forces. Drag (F_{x_2}) and lift (F_{z_2}) force values of sphere S_2 are presented in figures 14(*a*,*b*), respectively. Black lines with the values F_{x_0} and F_{z_0} are the drag and lift forces undergone by a single sphere without any interactions. They represent the forces that the sphere S_2 would have experienced without any interaction.

The evolution of the drag force shows that for type I, F_{x_2} is almost the same as the reference value. This result was expected since both spheres see almost the same free flow (with the difference of a slight impact of the S_1 shock wave on S_2). From SSI types I to IV, as S_2 goes down and interacts with the S_1 shock wave, F_{x_2} increases. It reaches a

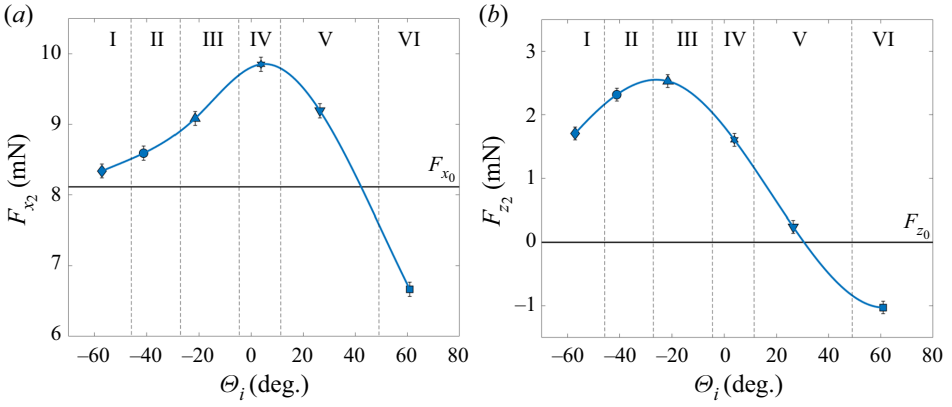

Figure 14. (*a*) Drag and (*b*) lift forces of S_2 measured with thrust device.

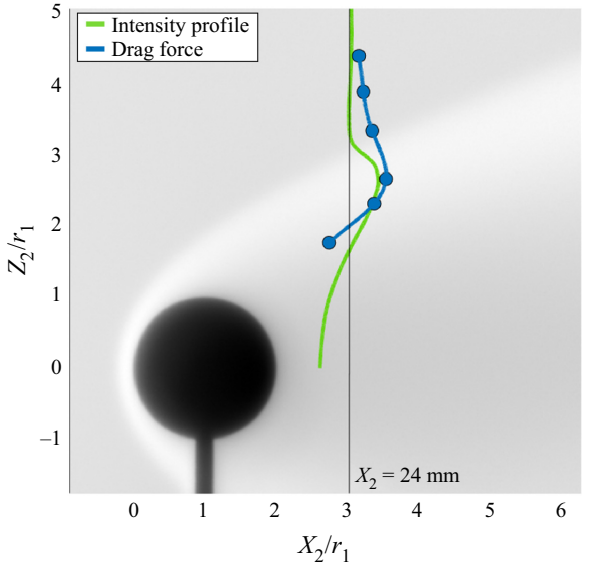

Figure 15. Drag force and luminous intensity profiles along the vertical axis $X_2/r_1 = 3$.

maximum for a type IV SSI, the transition area highlighted particularly in § 4.2. For types V and VI, the drag force suddenly decreases, reaching values lower than F_{x_0}. Again, this is due to the fact that S_2 goes deeper into the wake of S_1, where the flow is more rarefied, and presumably reaches speeds that are lower than the free-stream flow. As a result, the forces experienced by S_2 behind S_1 (in the x-direction) decrease greatly, suggesting that when a fragmented piece of debris remains behind a parent piece of debris, the latter protects it from being damaged by the free flow. In figure 15, the luminous profile along the vertical axis $X_2/r_1 = 3$, and the drag force profile, are plotted, both according to Z_2. Since the luminous intensity is the reflection of the local density, no recompression area is observed in the wake of S_1. Therefore, since the profile of the drag forces follows the profile of the intensity, the decrease of the altitude of the sphere S_2 leads to the decrease of the force F_{x_2}. This statement will be confirmed later in this work with the oscillating sphere results.

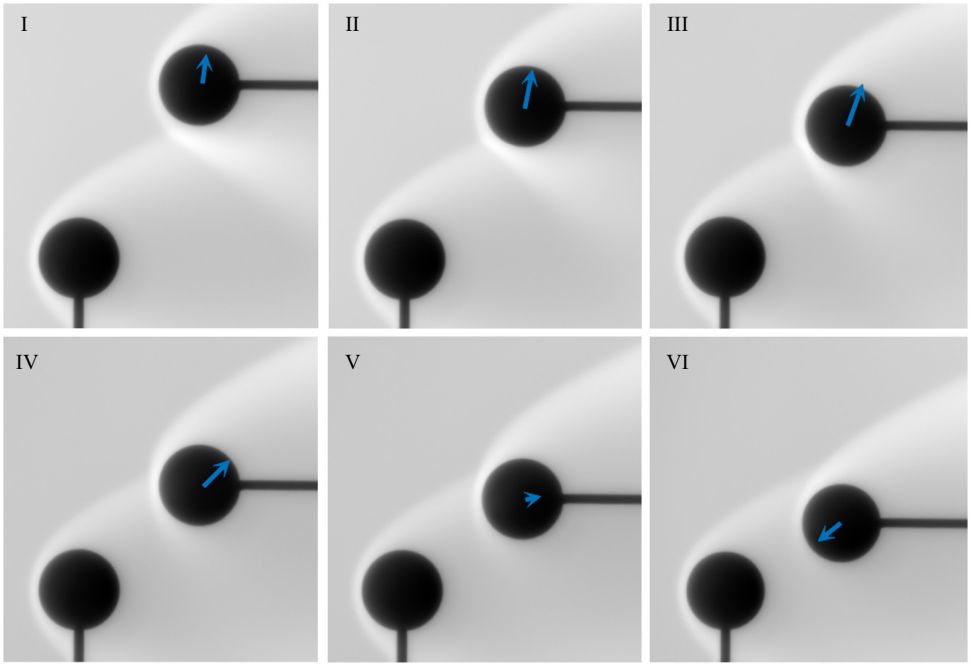

Figure 16. Calculated displacement of S_2 in S_1 reference frame according to the shock/shock interaction type.

With respect to lift forces, for types I–III, S_2 is mainly above the shock wave of S_1, and after, it is mainly below. Therefore, one would expect S_2 to be respectively repelled or attracted in the z-direction by ricocheting off the shock wave of S_1, as can be observed in the continuous regime (Register *et al.* 2020). But in fact, since the shock wave from S_1 is thick and diffuse, it does not represent a clear boundary that would block S_2 in the wake of S_1. For this reason, the sign of the lift force of S_2 does not change as it approaches the shock of S_1 from above or below, but simply decreases. Nevertheless, it could undergo a change of sign for a type VI SSI, but this would be due not to shock/impact interference but to the protection created by S_1, when S_2 is in its wake and close to the axis of S_1.

According to the forces undergone by S_2 and S_1, one can deduce the displacement of S_2 toward S_1 as follows:

(i) if $F_{x_2} < F_{x_0}$, then S_2 approaches S_1 in the x-direction ($\Leftarrow$)
(ii) if $F_{x_2} > F_{x_0}$, then S_2 moves away from S_1 in the x-direction ($\Rightarrow$)
(iii) if $F_{z_2} < F_{z_0}$, then S_2 approaches S_1 in the z-direction ($\Downarrow$)
(iv) if $F_{z_2} > F_{z_0}$, then S_2 moves away from S_1 in the z-direction ($\Uparrow$).

Taking into account both the values and directions of each force, the resulting forces were calculated in the S_1 referential, and the results are drawn in figure 16, giving information on the direction of S_2 towards S_1. As can be seen, when S_2 and its shock are enveloped in the shock of S_1, it is attracted to the first sphere.

4.3.2. *Comparison with the continuum regime*

Fisher (2019) studied the SSIs of Edney in a continuum regime at Mach 5. His experiment consists in releasing a sphere that flies freely in the flow field generated by a

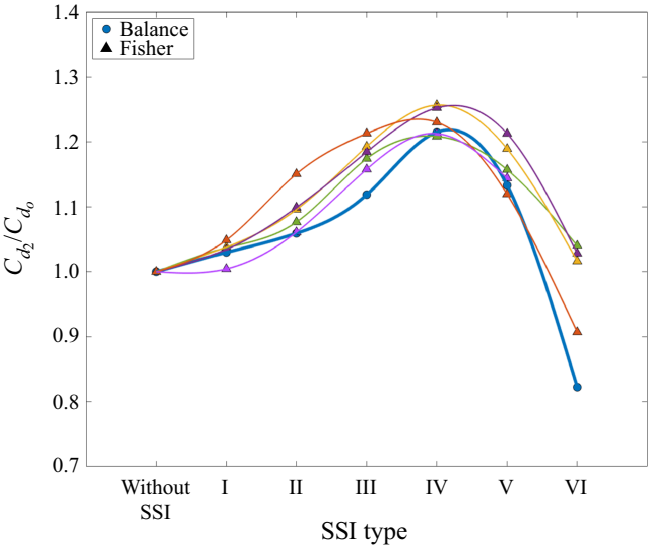

Figure 17. Drag coefficient of the present work on the vertical axis $X_2/r_1 = 3$, compared with the results of Fisher (2019), with variable coordinates.

primary sphere. This work allows us to compare SSI depending on the level of rarefaction, since drag forces were measured.

In the work of Fisher (2019), the drag coefficient was calculated with $C_d = \frac{1}{2}F_x/(\rho_\infty V_\infty^2 S)$, where ρ_∞ and V_∞ are the values in the free-stream flow (upstream of S_1), and $S = \pi(D/2)^2$. Note that this method does not take into account the local flow seen by S_2 moving in the flow generated by S_1. Since free-stream flow conditions impact directly the flow generated downstream of S_1, it is questionable if this parameter is effectively representative of the aerodynamics of S_2. Nevertheless, it allows us to compare results with the literature, where this method is mostly used. In our conditions, the drag coefficient of a single sphere is 1.35, while Fisher's is about 0.88. For both results, the drag coefficient of S_2 (C_{d_2}) is normalized by that of a single sphere (C_{d_o}). In figure 17, it is clear that the trends of all the curves are similar: for type I, the drag force of S_2 is almost that of the sphere alone in the free stream; in the wake of the sphere S_1, the dynamic pressure decreases as one moves towards the centre of the flow, i.e. towards a type VI interaction. The flow therefore becomes rarefied; the viscosity increases as well as the mean free path. As the local density and velocity decrease, the forces become smaller. The second sphere will experience weaker forces and, in a way, S_2 will be 'protected' by remaining in the wake of the first sphere, S_1. So the impact of the SSI, in terms of drag coefficients, is similar for both regimes. Nevertheless, this analysis has to be taken with caution for two reasons. On the one hand, the trajectory described by the sphere of Fisher is different from ours. On the other hand, the drag coefficients are given according to a type of SSI, but not in terms of location. As the shock wave of S_1 is thicker and more diffuse in a rarefied flow, the area where SSI occurs will be larger than in a continuum regime, expanding the area of high drag forces. This hypothesis seems to be confirmed by the results of Laurence & Deiterding (2011).

In figures 18(*a*,*b*), respectively, the drag and lift coefficients are plotted according to the normalized distance of S_2 towards the incident bow shock. Here, Z_2 is the altitude

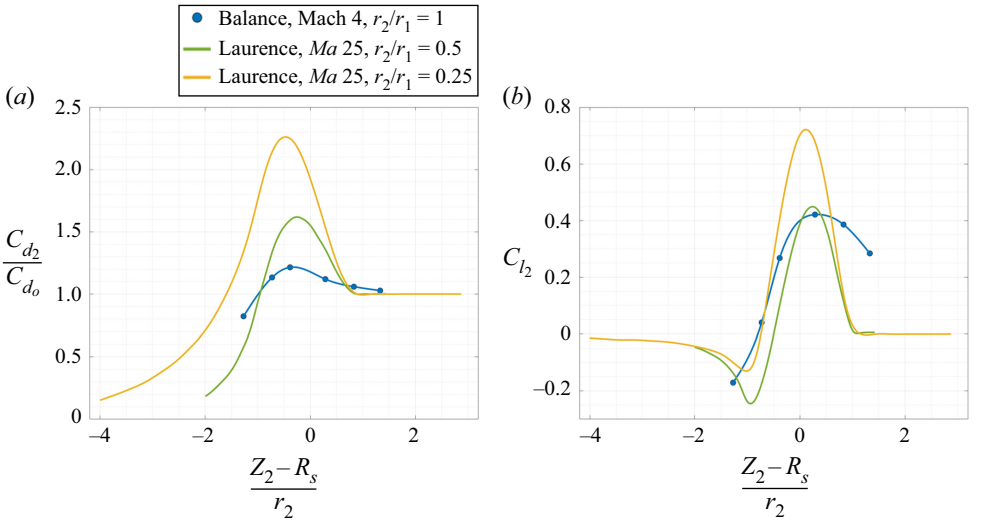

Figure 18. Drag and lift coefficients of the present work for a longitudinal distance of 1.5 diameters, compared with the results of Laurence & Deiterding (2011).

of S_2 towards S_1, R_s is the altitude of the shock wave (middle shock in our case), and r_2 is the radius of S_2. Both results concern the vertical axis $X_2/D_1 = 1.5$ ($X_2/r_1 = 3$). As far as drag is concerned, it can be seen that the maxima are obtained globally at the same location for all cases, but their amplitude varies inversely with the radius ratios of the spheres. The two iso-Mach curves have roughly the same shape, although they were obtained for different sphere radius ratios. This suggests that for ratio 1 , the corresponding curve would also have the same shape but would show a smaller maximum value. The curve obtained in the present work has a slightly different shape from the other two, with a wider curvature around the maximum, which could be due to rarefaction effects. However, this remains a hypothesis because it was performed at a lower Mach number. Regarding the lift coefficients, at iso-Mach, the maxima and minima have the same locations, and again with very similar shapes, as for the drag. Nevertheless, the maximum lift is observed for the same location, the curve does not have a minimum, and especially the shape of the curve around the maximum is less sharp and wider. This last point, observed for both the drag and the lift, might be due to the important decrease in Mach number, but in any case, if they exist, these effects are coupled with the increase in the rarefaction level that thickens the incident shock wave, and thus enlarge the area where the aerodynamic coefficients of S_2 are impacted.

4.4. *Surface pressure*

4.4.1. *Wall pressure analysis*

The pressure distribution at the surface of S_2 was measured for the same six locations as those already investigated. However, three other relative positions were explored to better describe the transitions between the different types of SSI, in particular between types III and IV, and between types IV and V. The pressures were also measured for a single sphere, representative of the reference wall pressure distribution. Figure 19 describes, for each type of SSI, the pressure distribution at the surface of S_2 in blue, along with the reference case in orange. The wall pressure values (p_p) are normalized with the stagnation pressure (p_0)

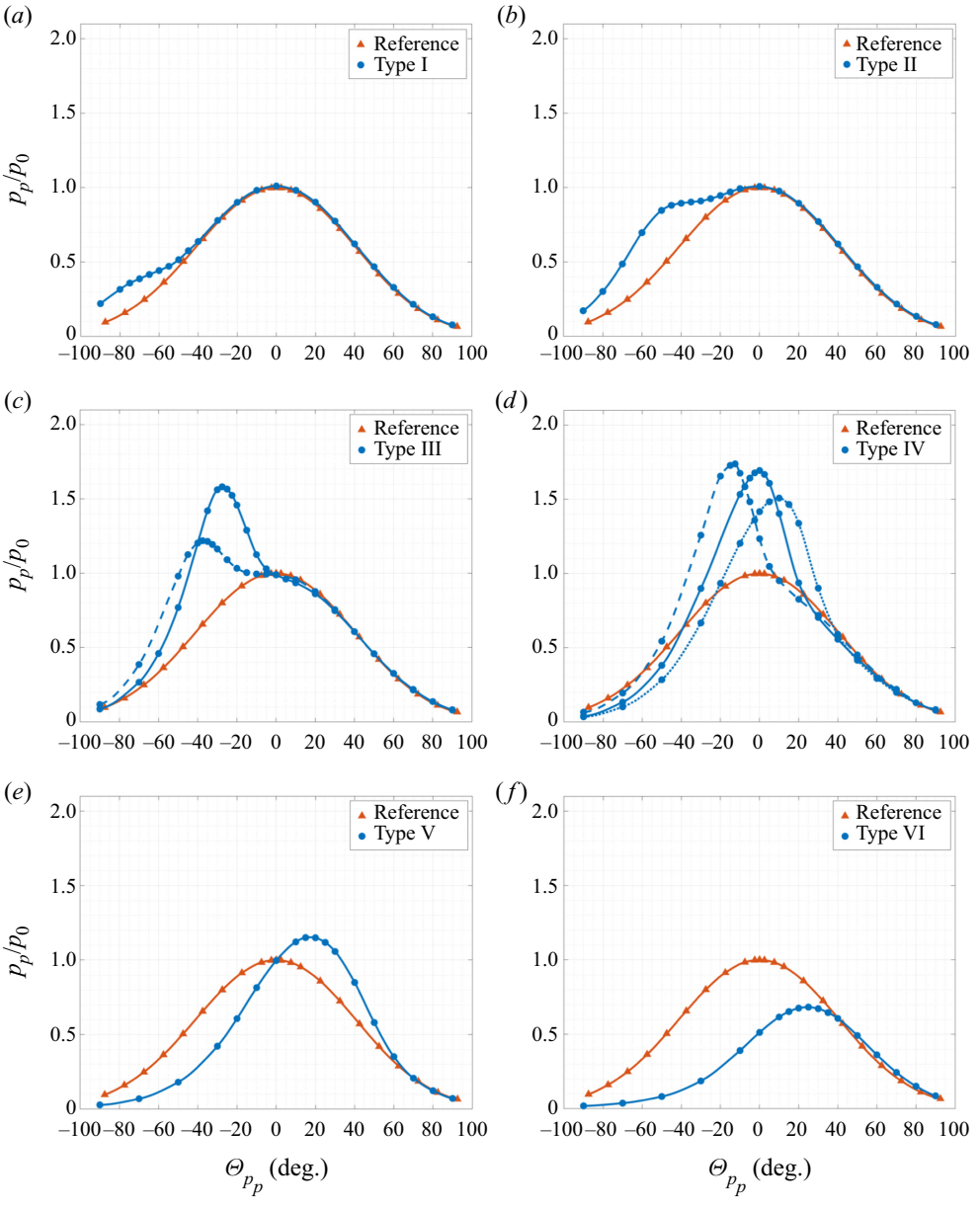

Figure 19. Pressure distributions for the six types of SSIs and for a single sphere (reference case).

which is 56.17 Pa. The wall pressure distributions are given as functions of the angle of the measurement point (Θ_{p_p}) with respect to the surface of S_2, 0° being taken with respect to the nose of the sphere.

The pressure distribution reveals two different behaviours. Concerning types I, II and III, the surface pressure is disturbed only on the lower part of the sphere ($\Theta_{p_p} < 0°$). For these three types, the wall pressure is higher than the reference case in the interference area. After this increase, the wall pressure returns to the reference behaviour. Pressure distribution clearly presents two peaks: one which corresponds to the intersection zone

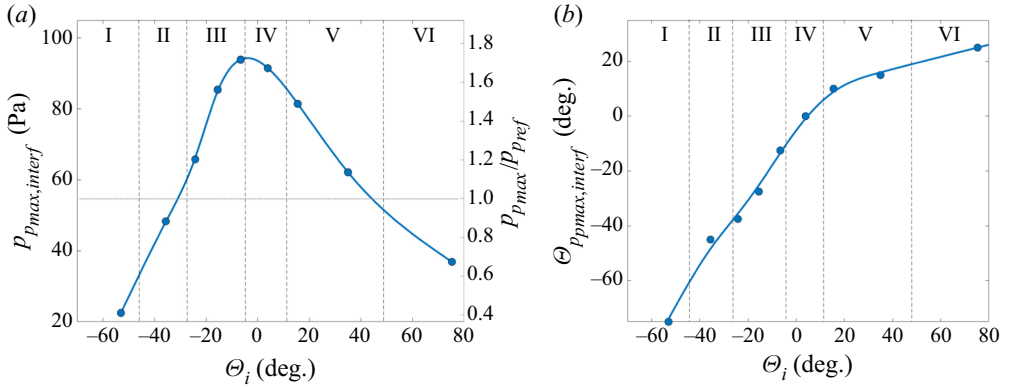

Figure 20. (*a*) Maximum surface pressure $p_{p_{max,interf}}$ and (*b*) its angle $\Theta_{p_{p_{max,interf}}}$ according to the interaction angle Θ_i.

of two shocks, and the other which corresponds to the nose of the sphere (at the stagnation point). In the first case, the peak is not, mathematically speaking, a maximum, but it is obtained with the minimum of the pressure derivative according to the angle, corresponding to the interaction area. For types IV, V and VI SSI, the pressure distributions are modified globally, resulting in only one maximum corresponding to the intersection area. Outside the interference area, in the lower part of S_2 ($\Theta_{p_p} < 0°$), values are lower than those of the reference case. At maximum, a great peak is reached, and then the slope tends to stick to the reference value. For types IV and V, the peak is clearly higher than the reference maximum value, while type VI is lower, which is coherent with the fact that S_2 penetrates deeper into the wake of S_1, i.e. when the flow is more rarefied.

Pressure peaks in the interference area ($p_{p_{max,interf}}$) are plotted according to Θ_i in figure 20(*a*). The angle of these peaks ($\Theta_{p_{p_{max,interf}}}$) are also plotted according to Θ_i in figure 20(*b*). Due to the thickness of the shock wave, the angles given as frontier (figure 10) are not clear delimitations; this is why the three positions of type IV presented in figure 19 are not located in the exact Θ_i range. Nevertheless, regarding the shape of the pressure distribution of the three points discussed for type IV, they seem to follow the same behaviour. With this assumption, we will henceforth consider them as representative of a type IV SSI. Figure 20(*a*) shows an increase from I to IV and then a decrease of the maximum pressure in the intersection area. The maximum pressure peak is reached when middle shock waves interact at approximately $-5°$ from the horizontal, which corresponds to a type IV SSI. Figure 20(*b*) plots the location of the pressure peak at the surface of S_2 as a function of the angle of the interaction point. As can be observed, the curve presents two distinct regions with two different slopes. The first area corresponds to types I to IV, where the value of $\Theta_{p_{p_{max,interf}}}$ increases until it reaches the same value as the angle of intersection. From this point, the curve has a gentler slope for types V and VI, since $\Theta_{p_{p_{max,interf}}}$ increases by 20° for an increase of Θ_i by 60°. One can notice that the maximum pressure is located mostly on the lower part of the sphere and does not seem to go higher than 25° from the stagnation point, even if the intersection angle is on the higher part of the sphere.

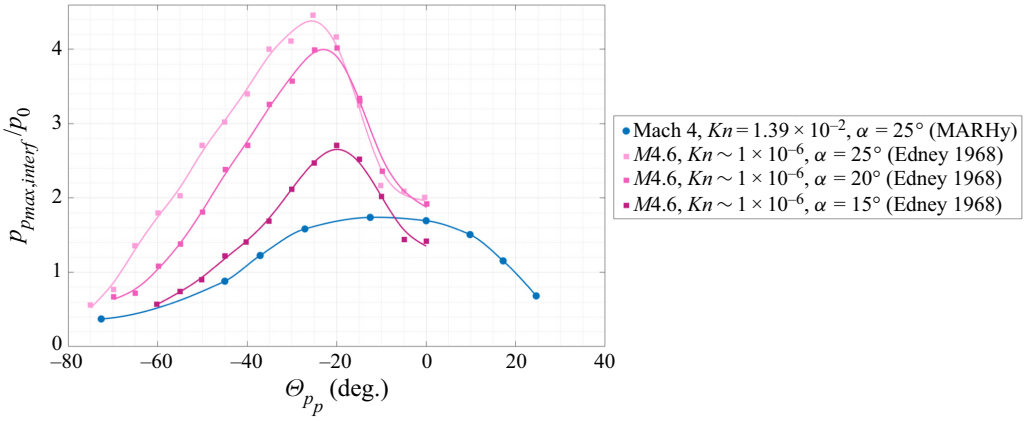

Figure 21. Pressure peak distribution, comparison with results of Edney (1968) in a continuum regime.

4.4.2. *Comparison with the continuum regime*

A comparison of the pressure distribution of the present work has been made with the results of Edney (1968) (see Appendix A). His work, based on the interaction of an oblique incident shock with the bow shock of a hemisphere, indicates a similar behaviour for SSI types I to III, with more pronounced pressures values, and thinner pressure peaks. The real difference is observed for SSI types IV to VI. In particular, the specific pressure distribution of the continuum regime seems to vanish completely in our rarefied conditions, appearing a lot like a type V or VI. This might be due to the thicker boundary layer that would prevent a supersonic jet from impinging at the wall of S_2. Thus the type IV interference might be disappearing as the level of rarefaction increases, as suggested by Gusev & Erofeev (2004) or White & Kontis (2018), who studied the impact of an incident shock on a cylinder at Knudsen numbers equivalent to our conditions.

Figure 21 focuses more specifically on pressure peaks. It is obvious, whatever the angle of incident shock, that the continuum case presents higher values of pressure peaks. Their repartition at the wall of S_2 is more localized: it concerns a region of about 10°, against 40° in our case. Also, the maximal pressure peak is located on a lower angle (about −25°) than the one that we observed in the rarefied regime (about −10°). These differences are consistent with the increase in the thickness of the shock wave due to an increase in the level of rarefaction: the impact of the SSI is localized not in one point, but in a zone leading to a decrease in the impact of the boundary layer of the second sphere at its surface, and therefore also the decrease in wall pressure.

4.5. *Discussion regarding the results obtained for* $X_2/r_1 = 3$

Analysis of the results presented in figures 11–14, 19 and 20 allows us to make several observations and analyse the different SSIs as follows.

(i) Type I does not impact S_2 much. The sphere is mostly located in the free stream and thus suffers more from it than from the interaction with the S_1 shock wave. Looking at the wall pressure distribution, it can be seen that the values are slightly higher in the interference area, located on the lower part of the sphere, which explains the lift force that is a bit higher than the reference.

(ii) Type II implies a recoil of the S_2 shock wave from its surface, at the nose of the sphere but also in the interaction area; only the BL seems to decrease. The local density in both areas also seems to increase, along with the drag force. The lift force also increases, but this is due to a greater modification ($p_{p_{max,interf}} \simeq p_0$) of the wall pressure on the lower part of S_2.

(iii) Type III shows the same tendency as type II. The stand-off distances reach a maximum (except for BL) for $\Theta_i \simeq -10°$, which corresponds to the angle of minimum distance of the BL in the interaction area. The drag force keeps increasing as S_2 goes down, while the lift force reaches a maximum $\Theta_i \simeq -20°$, and then decreases. Looking at the pressure distribution, it is noticeable that the great pressure peak ($p_{p_{max,interf}} > p_0$) displaces towards the centre of the sphere, decreasing the lift effect that had the incident shock for higher positions.

(iv) Type IV shows strong variation in shock distances. Stand-off distances decrease drastically to reach a minimum for $\Theta_i \simeq 20°$. A recoil of the interaction point and of the BL in the interaction area is observed, with local maximum for $\Theta_i \simeq 0°$. Then both decrease until their reference value. The BL seems less impacted than the MS. The maximum at $\Theta_i \simeq 0°$ also corresponds to a maximal density in the interaction area and at the nose of S_2. It also corresponds to a maximal drag force and a maximal pressure peak. The strong compression of the shock wave might be the reflection of the drag force and pressure maximum. After this specific location corresponding to $\Theta_i \simeq 0°$, the density, the forces and the pressure all decrease.

(v) Types V and VI are similar SSIs. They both present an increase in the stand-off distances, along with a decrease in the local densities corresponding to an increase of the rarefaction level since they entered the wake of S_1. The drag and lift forces decrease, even reaching values that are lower than the reference. The global modification of the wall conditions decreases the maximal pressure peak. For $\Theta_i > 40°$, the stagnation pressure is no longer reached, as for the reference drag force.

5. Drag force analysis with the swinging sphere experiment

In a previous study, Cardona & Lago (2022) explored the swinging sphere method (described in § 3.2.1) applied to a sphere moving in the wake of another one. The force measurements obtained previously with this method were compared to those obtained with another device: the aerodynamic balance (described in § 3.2.2). The validation of the swinging method shown in Appendix B will make it possible to explore other changes in the aerodynamics of debris when an interaction with other debris exists. This method can be applied on both the first and second spheres since this force measurement is non-intrusive.

5.1. *Impact of S_1 on S_2 aerodynamics*

To measure the impact of S_1 on S_2 aerodynamics, the swinging method was applied on a certain number of trajectories. The support of S_2, initially placed in a chosen position, is then moved in the x- or z-direction. In figure 22(a), the mean trajectories described by S_2 are plotted along with its mean drag force values. Values are given with maximum inaccuracy ± 0.6 mN, estimated with the dispersion of the measured points (see figure 33). Note that in the calculation of the drag forces with the swinging technique, we did not consider the lift forces. Since the maximal lift force is 2.5 mN, it represents 8.9 % of the sphere weight, which corresponds to maximal error 0.84 mN on the drag forces.

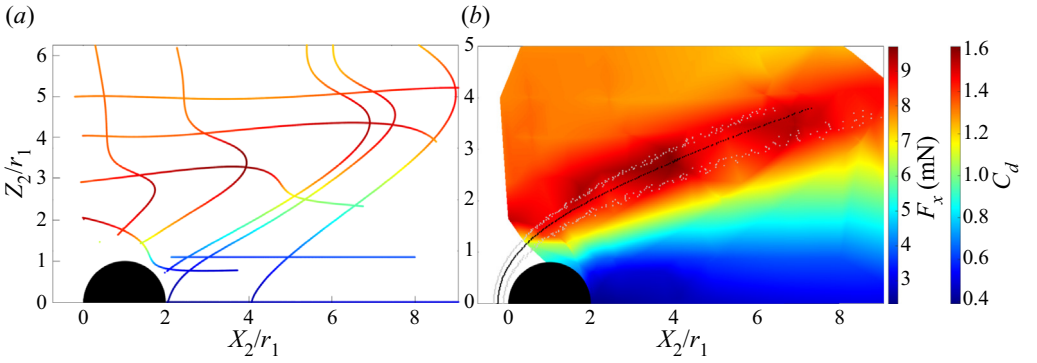

Figure 22. (*a*) Plot of S_2 mean drag forces according to location on the different swinging trajectories. (*b*) Interpolated mapping of the drag force and drag coefficient.

The mapping in figure 22(*b*) is obtained by interpolating these results. As can be observed, the mapping is not well defined, which is due to an insufficient number of measures. Nevertheless, it allows us to have first knowledge of the drag forces endured by a sphere in interaction with another. On the mapping are plotted the three regions of the S_1 shock wave. As can be seen, the maximum drag force is reached in the shock wave regions. When above the shock wave, the S_2 drag force is that of the reference case; when under, the S_2 drag force decreases until minimum value 2.4 mN. Except around the incident shock, there is no increase in F_x. This confirms that, due to the rarefaction level, there is no recompression wave in the wake of S_1. This marks a great difference with the continuum regime.

With the use of the swinging method, we can also observe some behaviours in the wake of the S_1 flow. Looking at the swinging trajectory where S_2 is displaced horizontally in the x-direction ($Z_2/r_1 = 0$), no change of drag forces is observed. If there were some recirculation, then we should have observed, at one point, a change in the sign of the angle of S_2 wires, S_2 being pushed towards S_1 by the recirculation. As this is not the case, we might think that there is no recirculation behind S_1. This hypothesis would be consistent with previous studies from the literature, where numerical and experimental studies were carried out to understand the evolution of the wake structure of a sphere, under hypersonic and rarefied flow conditions with Reynolds numbers ranging between 194 and 2129. Experimentally, the wake of a sphere was analysed with Pitot pressure measurements and hot wire velocities (Muthoo & Brundin 1974). The numerical works were carried out with the direct simulation Monte Carlo method, some test cases of which were validated by the experimental results (Reeves & Lees 1965; Dogra *et al.* 1994). All the results showed that the wake shows neither separation nor recirculation in the range of Reynolds numbers studied by the different authors. The same conclusions can be applied to our experimental conditions where the Reynolds number is 294.5.

As explained in Appendix B, to validate the swinging method, some measurements were realized with the aerodynamic balance on a chosen trajectory: initial position ($X_2/r_1 = 2$, $Z_2/r_1 = 0$) and support moved up. Thanks to these measurements, we obtained the drag, but also the lift forces on this trajectory. Figure 23 presents their values (yellow squares) according to the normalized vertical distance of S_2 towards the middle shock. The value obtained for $X_2/r_1 = 3$ have been superposed to evaluate the evolution of the drag and lift forces according to the longitudinal distance. As can be observed, the variation of the

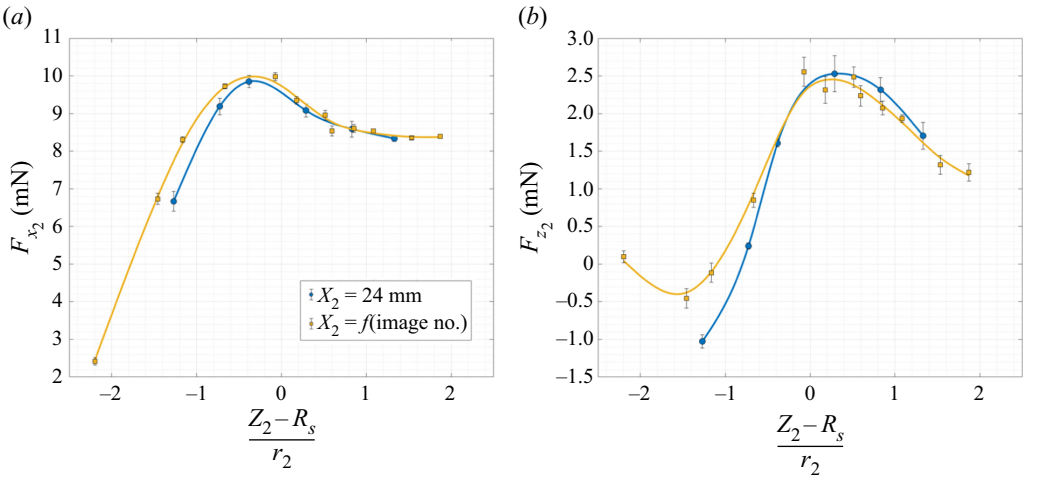

Figure 23. (*a*) Drag and (*b*) lift forces of S_2 on the swinging sphere trajectory ($X_2 = f$(image no.)) and on the vertical axis $X_2 = 24$ mm ($X_2/r_1 = 3$).

longitudinal distance ($X_2 = f$(image no.)) does not affect much the distribution of forces towards the middle shock of S_1. For both the drag and the lift, only a slight increase in the values is observable when S_2 is located under the S_1 shock wave.

Figure 24 shows the locations of S_2 where we measured the results of figure 23. It can be seen that the only point corresponding to $X_2/r_1 < 3$ is the lowest one ($(Z_2 - R_s)/r_2 = -2.2$). This means that the increase in drag is due to an increase in the diffusion of the S_1 shock wave as we look downstream, impacting S_2 aerodynamics on a wider area. Nevertheless, the diffusion of the S_1 shock wave downstream also implies a decrease in the local pressure in the shock wave. This is why we observe lower negative lift on the low position of S_2, and lower positive lift on the higher position of S_2. Nevertheless, the little impact of the longitudinal distance of S_2 shows that the flow field generated by S_1 can affect a following object in a wide area.

Thanks to the drag and lift measurements, in figure 24 are also plotted the local displacement of S_2 towards S_1. From $Z_2/r_1 = 0$ to the transition between types VI and V, the second sphere seems attracted by S_1. As shown in § 4.4, for this type VI SSI and lower position, the maximal wall pressure is lower than the reference case due to a higher local rarefaction level. As there is no observed recompression area, S_2 is less repulsed than S_1 in the x-direction, and so they will remain close to each other. Also, as the repartition of pressure is located mostly on the upper part of S_2, it is pushed downwards. So S_2 also gets close to S_1 in the z-direction.

Between types VI and V, the results seem to show that there is a transition zone where the direction of S_2 reverses. Referring to the different data for the position of $X_2/r_1 = 3$ and $\Theta_i \simeq 40°$, we observed in § 4.5 that the local density (figure 13*b*), the drag and lift forces (figure 14), and the pressure peak (figure 20) all reach values equal to those in the reference case. At this particular position, S_2 does not move relative to S_1, so the two spheres follow the same flight path. It is possible that these specific flight conditions lead to an equilibrium position, where S_1 and S_2 fly together without moving away from each other. As the wall pressure distribution around the sphere S_2 is not axisymmetric, one could think that a skin friction effect located on the lower part of the sphere could compensate the wall pressure forces located on the upper part of the sphere, leading to a local equilibrium.

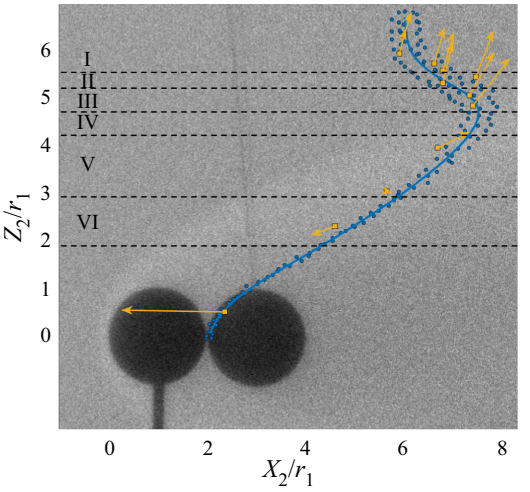

Figure 24. Calculated displacement (yellow arrows) of S_2 in the S_1 reference frame according to its position on the swinging trajectory (blue line).

This effect seems to be confirmed by the behaviour of type V SSI measurements. By analysing further the pressure data of this interaction, we calculated that 66 % of the wall pressure contribution corresponds to the half-sphere on the upper part of S_2, which is still not consistent with a positive lift. In the continuum regime, the lift forces are driven mostly by the pressure contribution. However, in the present case, results seem to suggest a strong implication of the viscous effects, still not well understood, marking a difference with the continuum regime. It is probable that the viscous effects might act mostly on the lower part of S_2, balancing the wall pressure that acts on its upper part, leading to a positive lift. Then, from type IV to I and beyond, S_2 is pushed away from S_1 in the x- and z-directions. In the x-direction, this is understandable since wall pressures are higher than the reference case. In the z-direction, since pressure peaks are located on the lower part of S_2 for type III to I, we also easily understand the positive lift forces.

5.2. *Impact of S_2 on S_1 aerodynamics*

Whether in hydrodynamics (Zhu, Liang & Fan 1994) or aerodynamics (Golubev 2012), studies demonstrated that the location of S_2 around S_1 impacts directly the drag forces endured by S_1. The swinging method being a non-intrusive way to measure drag forces, it can be applied to S_1 with the presence of S_2 in its flow. In this way, we can observe the behaviour of S_1 while moving S_2 longitudinally on the axis $Z_2/r_1 = 0$, and vertically on the axis $X_2/r_1 = 3$, to complete our study.

5.2.1. *Case $Z_2/r_1 = 0$*

The sphere S_2 was first displaced on the horizontal axis ($Z_2/r_1 = 0$), which corresponds to the study by Golubev (2012). Four locations of S_2 were studied, and the results are given in figure 25. Here, we present the drag force measured for the swinging sphere S_1 according to the relative position of S_2. Figure 26 shows the normalized enhanced images corresponding to these positions. They allow us to better understand the physics of the flow field, since they are compared to images of a single sphere in the flow.

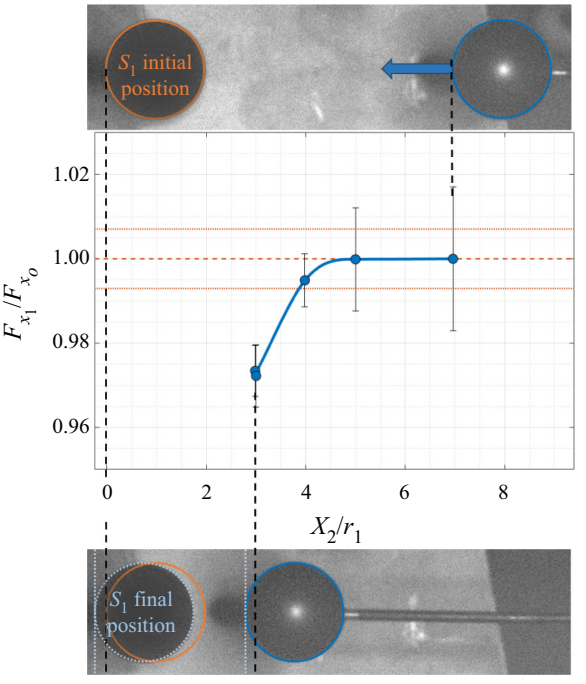

Figure 25. Drag forces of S_1 according to X_2, the position of S_2 relative to S_1 in the x-direction ($Z_2/r_1 = 0$).

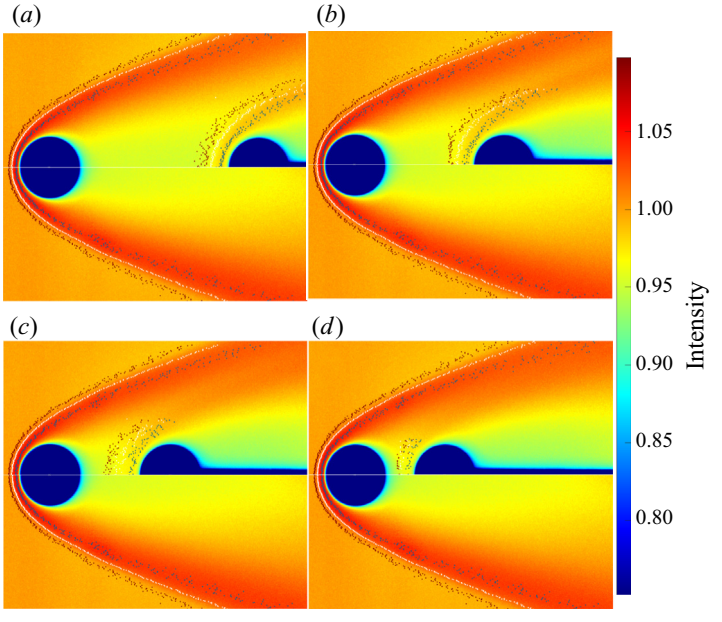

Figure 26. Normalized images with jet colour map and detection of shock waves. Top images of (*a–d*) show $X_2/r_1 = 7, 5, 4, 3$ mm, respectively, and $Z_2/r_1 = 0$. Bottom images show single sphere.

As observed in figure 25, when S_2 is far behind S_1, the latter is confronted by the same drag force as when it is alone in the flow. As S_2 gets closer, it reaches a point (around $X_2/r_1 = 4.6$) where it begins to affect the aerodynamics of S_1. Gradually, the S_1 drag force decreases. By observing the images of figure 26, a few things are noticeable.

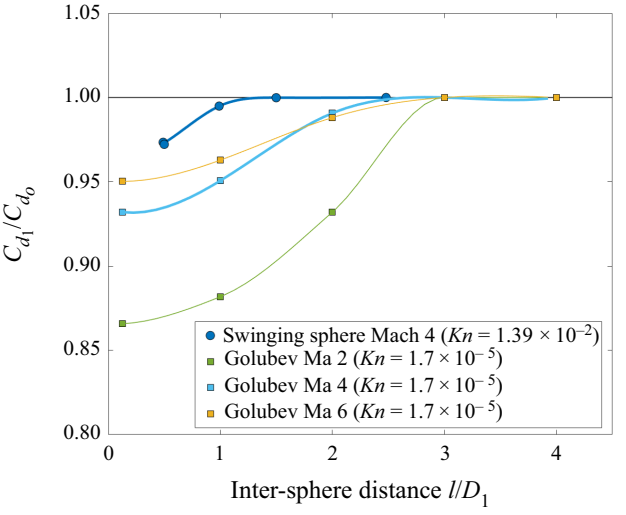

Figure 27. Dimensionless drag force of S_1 according the dimensionless distance between spheres l.

When S_2 is far enough from S_1 (figures 26*a*,*b*) not to disturb the S_1 drag force, it seems that the wake S_1 is not modified in at least the first diameter behind it. The S_2 compression wave is visible and shows the sign of a highly rarefied flow, with a great thickening of the wave and a great stand-off distance: 6.7 mm for figure 26(*a*), and 5.8 mm for figure 26(*b*). As S_2 gets closer to S_1 and enters a more rarefied flow with a lower velocity, the shock wave of S_2 has difficulty developing, but a compression is still visible upstream of S_2. The few molecules that constitute this compression might create a viscous layer that pushes S_1 upstream. Another point that might induce the variation of drag force is the merging of the incident shock with the compression wave induced by S_2.

Golubev (2012) calculated the S_1 drag force in a continuum regime. His results, shown and compared to ours in figure 27, were obtained for different Mach numbers but the same Reynolds number. In the continuum regime, the inter-sphere distance for which the drag coefficient of S_1 has a value equal to the reference is the same, whatever the Mach number. These three curves also show that the influence of the presence of S_2 is all the more important as the Mach number decreases. The curve obtained in this work, at Mach 4 in the rarefied regime, shows that the distance for which the drag coefficient of S_1 has a value equal to that of the reference drag is greater than that obtained at the same Mach number in the continuum regime. Comparison of the iso-Mach curves also shows that the slopes show that the influence of S_2 is substantially the same; meanwhile, the value of the normalized drag coefficient of S_1 is greater in the continuum regime.

5.2.2. *Case* $X_2/r_1 = 3$

In the same manner as for the previous case, S_2 is moved behind S_1, this time vertically on the axis $X_2/r_1 = 3$. Results of the measured S_1 drag force are plotted in figure 28 according the position of S_2. First, S_2 is placed so that it does not act on S_1, which does not displace itself. As S_2 is moved down, and gets closer to S_1, the swinging sphere moves ahead, as it does when S_2 is close behind it on the axis $Z_2/r_1 = 0$. With the normalized enhanced images of figure 29, an analysis equivalent to that from the case $Z_2/r_1 = 0$ can

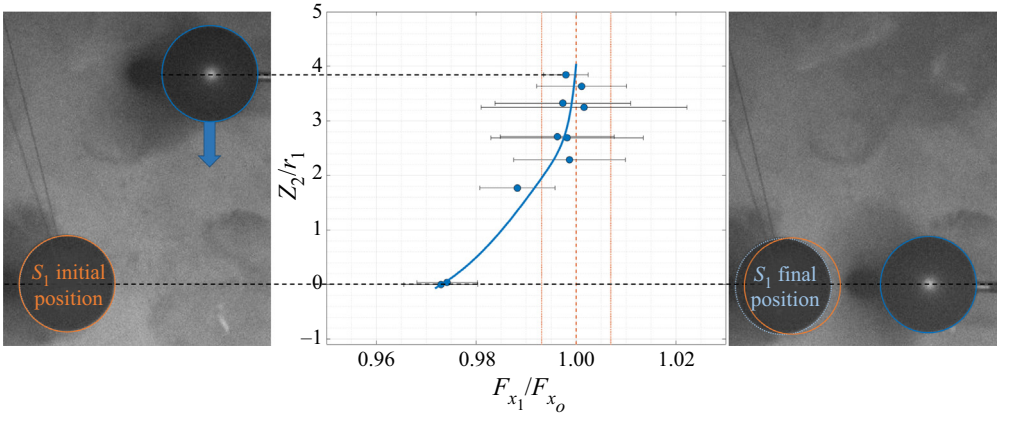

Figure 28. Drag forces of S_1 according to the position of S_2 in the z-direction ($X_2/r_1 = 3$).

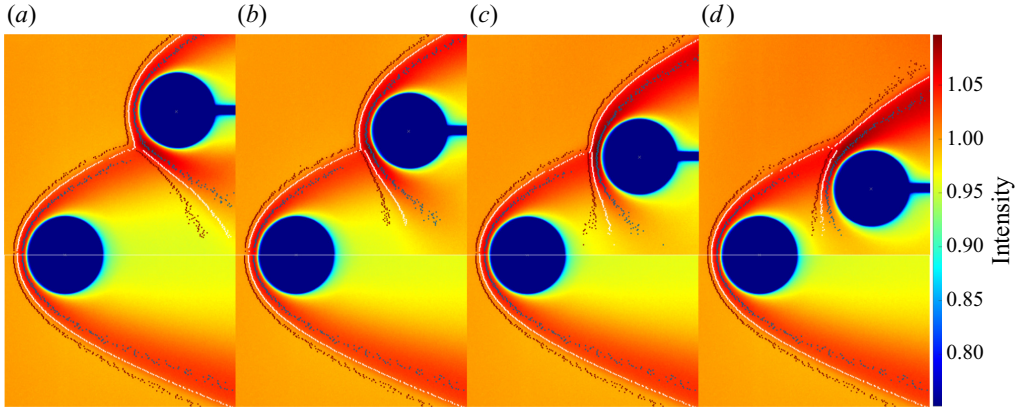

Figure 29. Normalized images with jet colour map and detection of shock waves. Top images in (*a–d*) show $Z_2/r_1 = 3.77, 3.25, 2.59, 1.74$ mm, respectively, and $X_2/r_1 = 3$. Bottom images show single sphere.

be made. As S_2 gets down, the lower part of the S_2 shock wave modifies the wake of S_1 by intensifying the density in its wake.

The cases where S_2 locations generate SSIs do not seem to affect the drag of S_1. Indeed, we observe 3 % of drag variation whether for displacement in the axis $Z_2/r_1 = 0$, where there is no SSI, or in the axis $X_2/r_1 = 3$, where there is. This variation is not really significant, but is still interesting. In the case of space debris re-entry, it would mean that the aerodynamics of a parent piece of debris, and thus its trajectory, depends on the location of the fragments debris. These fragments can be a single object, but more often they are clouds of fragments for which the modification of S_1 aerodynamics might not be negligible.

6. Conclusion

This work presents an experimental investigation of SSIs between two spheres in a supersonic slip regime. The purpose was to analyse the influence of viscous effects on the interference properties first described by Edney (1968), and still much studied today, particularly in the continuum regime.

These experiments were carried out in the MARHy wind tunnel, and many results were obtained in a supersonic rarefied flow. Free-stream conditions result in a Mach 4 steady flow with static pressure 2.67 Pa, corresponding to the rarefaction degree of fragmentation altitudes. Considering debris that fragments at 76 km altitude, the models used represent two spheres of about 1 m diameter interacting with each other. This study allowed a better understanding of the different types of SSIs, and of their effects on the aerodynamics of space debris re-entry.

This study is divided into two main parts:

(i) the analysis of SSIs for a fixed longitudinal distance that induces a constant incident shock angle of 25°
(ii) the analysis of the drag forces with the swinging sphere experiment.

Despite the rarefaction effects, the patterns of SSI described by Edney (1968) are still observed in our conditions. Nevertheless, our experimental visualization technique does not allow us to observe any supersonic jet or recompression wave in between the shock and the surface of the interacting object. The distribution of wall pressure tends to confirm that there is no jet impinging at the surface of the sphere, since the particular distribution of the type IV SSI seen in the continuum regime vanishes in our conditions.

Concerning the wall pressure, some differences should be pointed out: the distribution is smoother, with lower pressure peaks. It is to be noted that for type V and VI SSIs, the pressure peaks are lower and localized on the top of the sphere, while in the continuum regime, they are higher than the reference value and concentrated at the nose of the sphere. This might be due to a recompression wave, non-existent in our case, that might be more impacting than the SSI itself.

As the SSI patterns seem to deviate from their original description in the continuum regime, it was desired to deepen the physics that explains these differences. Based on a drag forces comparison with the continuum regime, it is shown that their basic trends are similar; but due to our rarefaction level, the incident shock is thicker, which induces a smoother distribution of drag forces around the incident shock wave. According to the type of interference, the evolution of the drag force follows that of the wall pressure peak. This suggests that the drag force is influenced mainly by the pressure forces. Unfortunately, to our knowledge, there is no study in the continuum regime that would enable us to evaluate the viscous effects.

The measurement of the lift forces showed a larger area of influence around the incident shock than in the continuum regime. This demonstrates the viscous effects that are due to the thickening of the shock wave.

Another relevant behaviour of rarefied flows was observed. In some cases, we measured a positive lift force, while the pressure load was localized on the top of the sphere. This is due to skin friction on the bottom of the sphere that is large enough to compensate for pressure forces.

The complementary study realized with the swinging sphere experiment demonstrates that there is no recompression wave or recirculation area in the wake of the first sphere. It also shows that the second sphere, when at a distance less than $1.3D_1$, has little influence on the drag force of the first sphere, decreasing its value by 3 % when they are close to each other, thus increasing slightly its velocity. This drag variation is not observed when SSIs are observed, which means that they are due only to wake effects.

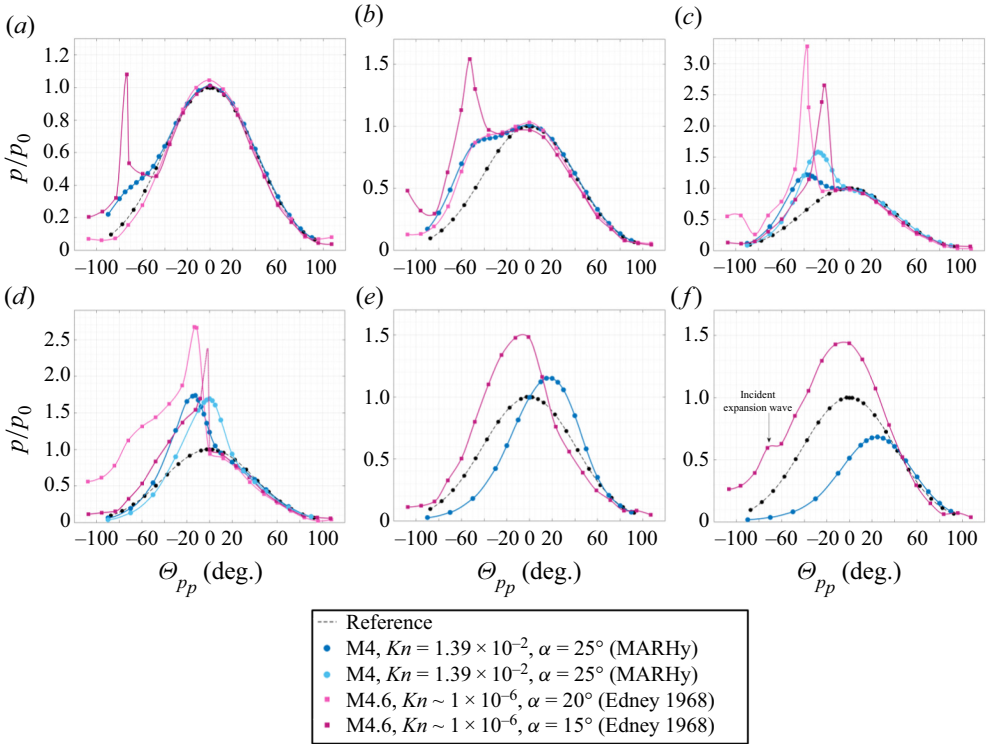

Figure 30. Pressure distribution, comparison with results of Edney (1968) in a continuum regime.

The results have shown a certain amount of differences with the continuum regime, which demonstrates the value of such experimental results in a rarefied flow.

Acknowledgements. Special thanks to H. Noubel and J.E.M. Morales for their advice on technical aspects and numerical simulation.

Funding. This work is part of a PhD fully financed by the Agence Nationale de la Recherche for the project IPROF: ANR-19-CE39-0003-01.

Declaration of interests. The authors report no conflict of interest.

Author ORCIDs.
Vincente Cardona https://orcid.org/0000-0002-6325-947X;
Viviana Lago https://orcid.org/0000-0002-5238-0370.

Appendix A. Pressure distribution: comparison between the continuum and the rarefied experiments

The graphs of figure 30 show the experimental results of the present study, superposed with those of Edney (1968). Both are the distribution of pressure at the wall of a sphere in interaction with an incident shock. Contrary to the present results, the incident shock of Edney is not a bow shock, but an oblique one.

Some differences should be pointed out for all six types of SSI: the distribution is smoother, with lower pressure peaks.

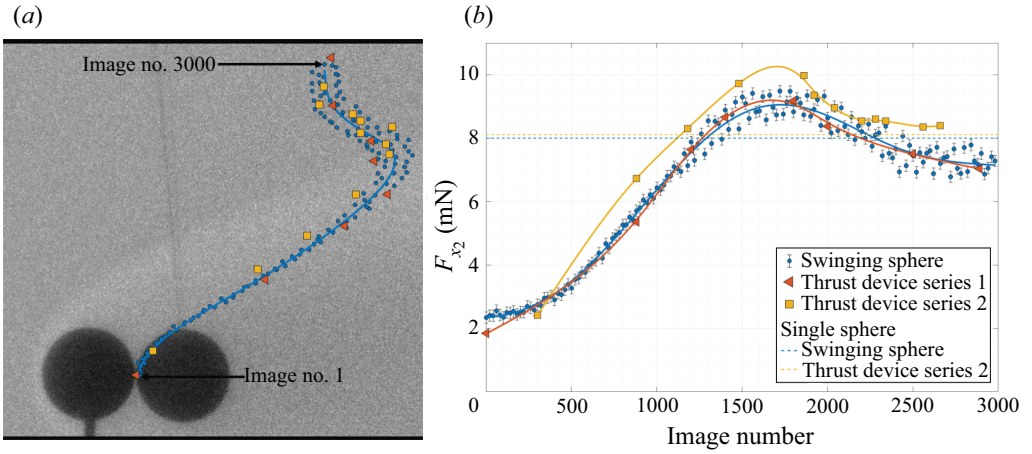

Figure 31. (*a*) Trajectory of the stagnation point of the swinging sphere, and location of the stagnation points of S_2 with the thrust device. (*b*) Drag forces according to the position of S_2.

The main difference is observed for type IV to VI SSIs. In particular, for type IV, the specific pressure distribution of the continuum regime seems to vanish completely in our rarefied conditions, making it look a lot like type V or VI. This might be due to the thicker boundary layer that would prevent a supersonic jet from impinging at the wall of S_2. Thus the type IV interference might be disappearing as the level of rarefaction increases, as was suggested by Gusev & Erofeev (2004) and White & Kontis (2018), who studied the impact of an incident shock on a cylinder at Knudsen numbers equivalent to our conditions.

For type V and VI SSIs, the pressure peaks are lower and localized on the top of the sphere, while in the continuum regime, they are higher than the reference value and concentrated at the nose of the sphere. This might be due to a recompression wave, non-existent in our case, that might be more impacting than the SSI itself.

Appendix B. Validation of the swinging sphere method on the second sphere

The swinging method was first validated in Cardona & Lago (2022), with the measurement of a single sphere suspended in the free-stream flow described in table 1. Results were compared to the literature, and measured drag forces were in accordance with those of Aroesty (1962), Bailey (1966) and Wegener & Ashkenas (1961). However, this method has not yet been validated by comparison with force measurements obtained with the aerodynamic balance. The pendulum method makes it possible to determine the value of the drag forces in the case of a sphere suspended in a known flow. The experiment consists of moving the sphere S_2 vertically; its angular displacement will depend on the properties of the flow surrounding it. The displacement of the sphere S_2 is done in the $Y_2 = 0$ plane, i.e. S_2 moves in the $\boldsymbol{x}$- and $\boldsymbol{z}$-directions. Figure 31(*a*) shows the two spheres at their initial position, and the trajectory described by the sphere S_2 is indicated by the blue points. 'Image no. 1' corresponds to the initial position of S_2, with both spheres aligned on the $\boldsymbol{x}$-direction, and 'Image no. 3000' corresponds to its final position. The image number increases with the altitude (Z_2-coordinate) of S_2.

To validate the measurement of the drag forces obtained by this method, measurements with the aerodynamic balance were carried out for the positions of S_2 marked with orange and yellow points on the trajectory, following two different protocols.

Before detailing the protocols, however, it is first necessary to explain how, experimentally, the flow conditions can be affected by the presence of objects in the flow core. As already mentioned, the free-stream flow in the isotropic core depends on the stagnation pressure p_0 and on the free-stream pressure p_∞. The pressure p_0 is adjusted at the beginning of the experiment and remains constant without being affected by the presence of objects in the flow. The pressure p_∞ of the free jet, on the other hand, depends on the obstruction of the core of the flow and can be adjusted with the butterfly valve that separates the test chamber and the pumping unit. Consequently, for a system with two objects, when one is moved in the flow, the free-stream pressure may vary slightly because the obstruction of the core flow is modified. For this particular swinging sphere experiment, images were acquired while the sphere S_2 was in motion, which implies that the pressure p_∞ changed slightly between the starting position, S_2 behind the sphere S_1, and the final position, 'Image no. 3000'. In the case presented here, the free-flow pressure was regulated with both spheres in the initial position, as shown in figure 31(*a*). This can produce a small uncertainty in the measurement of the force with this method.

To evaluate the influence of the pressure p_∞ on the measurement of aerodynamic forces, it was decided to adopt two protocols for the measurement of drag forces with the aerodynamic balance. They differ in the way the free-flow pressure was set: for measurements of series 1, the free flow pressure p_∞ was adjusted at the beginning of the experiment when the two spheres are in their initial position ('Image no. 1'), then p_∞ evolved freely according to the position of S_2. The experimental conditions of this first series are equivalent to those of the swinging method. A second series of measurements was made but, this time, for each position of the sphere S_2, p_∞ was adjusted and set at the nominal value (see table 1).

The three sets of drag forces measured – on the one hand with the swinging method, and on the other hand with the aerodynamic balance for series 1 and 2 – are plotted on the graph in figure 31(*b*).

As can be seen, the trend of the three curves is the same. A dispersion is observed in the measured force values (blue circles), which increases as the sphere S_2 approaches the passage of the shock created by sphere S_1. This is due to a slightly oscillating movement of the sphere S_2 that is observed during the experiments and which gives maximum deflection 0.6 mN. It should be noted that when the sphere S_2 is in the wake of S_1, this dispersion is almost no longer observable as shown in the figure. Series 2 shows greater values than the other two, which are in good agreement with each other. Both protocols show the importance of the variation in free-stream pressure. An interesting point to note is at the end of the trajectory of the sphere S_2, for image numbers above 2500. In figure 31(*b*), the two dashed lines give the value of the drag force of a single sphere measured with the swinging sphere experiment (blue) and with the aerodynamic balance (yellow). From image no. 2500, S_2 is not in direct interaction with the shock wave of S_1: the two shock waves still interact, but the incident shock does not impact the surface of S_2. Thus the aerodynamics of S_2 is almost the aerodynamics of a single sphere in free-stream flow. Besides, regarding series 2, it can be observed that the curve tends to reach an asymptote with the value of a single sphere, which is not the case for the other measurements.

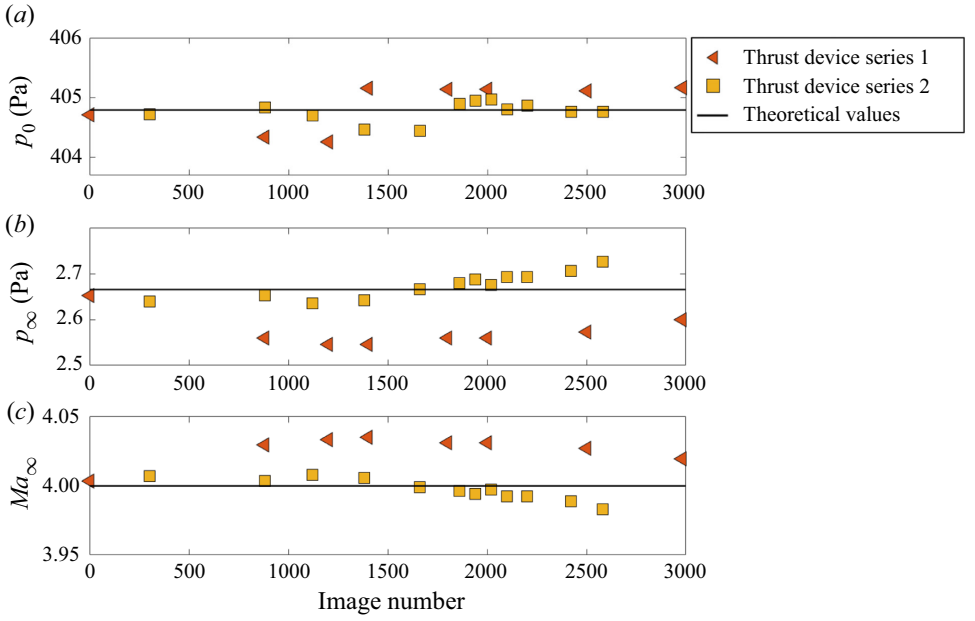

Figure 32. (*a*) Stagnation pressure p_0, (*b*) free-stream pressure p_∞, and (*c*) free-stream Mach number Ma_∞, for different positions of S_2.

In order to deepen the analysis of the impact of free-stream parameters on the measurement of drag forces, the stagnation pressure (p_0), free-stream pressure (p_∞) and free-stream Mach number (Ma_∞) are plotted for the two aerodynamic balance series measurements in figure 32. The free-stream Mach number is calculated with both pressures as

$$Ma_\infty = \sqrt{\frac{2}{\gamma - 1}\left[\left(\frac{p_\infty}{p_0}\right)^{(\gamma-1)/\gamma} - 1\right]}. \tag{B1}$$

As can be seen, the pressures and thus the Mach number of series 2 are close to the theoretical values, as desired for this experiment (see table 1). The last two points, near image no. 2500, are the farthest from the theoretical values. At this position, the drag forces of S_2, which is located in the free-stream flow described in table 1, should have the same value as for a single sphere. The small difference (0.2 mN) observed in figure 31 might be due to this tiny deviation in free-stream pressure, or to the fact that S_2 is still under a slight influence of the shock wave of S_1. However, the results of series 2 are in good agreement with what was expected, contrary to those of the swinging sphere experiment and the balance series 1, which present a difference of 1 mN with the expected drag value. While it is unsurprising to observe smaller values when the free-stream pressure is lower than expected (see p_∞ in figure 32), it is important to note that the pressure variations are small.

In table 2, we present the average values of flow pressures (p_0 and p_∞) and Mach number of series 1 and 2. This table also includes the differences ($\neq$) calculated with respect to the theoretical values. It can be seen that the free-stream pressure of series 1 is 3.41 % smaller than the nominal values, which is ten times the

			Series 1		Series 2	
		Theoretical (th.)	Value	$\neq$ with th. (%)	Value	$\neq$ with th. (%)
p_0	Mean (Pa)	404.792	404.878	0.02	404.765	0.01
	Std (Pa)		$\pm$0.388		$\pm$0.167	
	Std (%)		$\pm$0.10		$\pm$0.04	
p_∞	Mean (Pa)	2.67	2.575	3.41	2.675	0.34
	Std (Pa)		$\pm$0.036		$\pm$0.028	
	Std (%)		$\pm$1.40		$\pm$1.05	
Ma_∞	Mean (Pa)	4	4.026	0.65	3.997	0.08
	Std (Pa)		$\pm$0.010		$\pm$0.008	
	Std (%)		$\pm$0.26		$\pm$0.20	

Table 2. Mean pressures and Mach number compared to theoretical values.

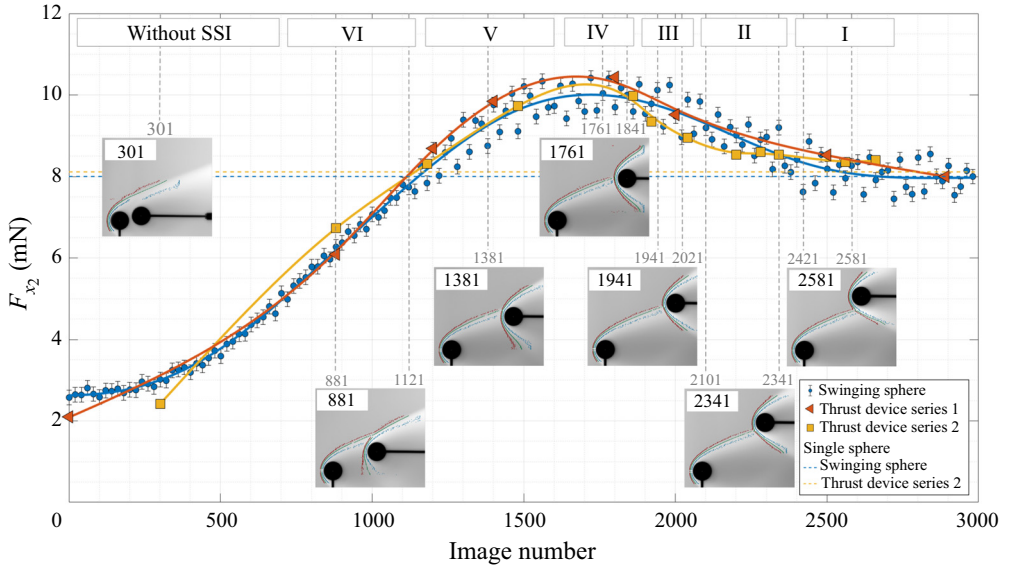

Figure 33. Drag forces rescaled with infinite value according to the position of S_2, and associated images.

difference calculated for the measurements of series 2. This 3.41 % decrease in free flow pressure, which could be considered acceptable, results in a 12.5 % decrease in the drag force measurement, which is a fairly significant error. Moreover, the Mach number increases by only 0.65 %, which is very little compared to the accuracies of experiments reported in the literature. Nevertheless, it seems that in these flow conditions, even variations considered negligible have, in fact, a great impact on measurements.

It is known that when S_2 is out of the shock wave of S_1, its drag force is equal to the drag force of a single sphere in the free-stream flow. Thus the measured forces of series 1 were corrected by rescaling values with respect to the value of a single sphere. In this way, the graph in figure 33 is obtained, showing three superposed curves. This means that with one known value, the swinging method can give exploitable drag forces.

Appendix C. Nomenclature

α	Angle of the wire (deg.)
Δ	Shock stand-off distance (m)
λ	Mean free path (m)
μ	Dynamic viscosity (Pa s)
ρ	Density (kg m^{-3})
Θ_i	Interaction angle (deg.)
Θ_{p_p}	Pressure measurement angle (deg.)
ς	Similarity number
A	Reference area (m^2)
C_d	Drag coefficient
C_l	Lift coefficient
D	Sphere diameter (m)
d_i	Distance between the intersection point and the surface of the sphere (m)
d_{ml}	Distance between the most luminous point and the surface of the sphere (m)
F_x	Drag force (N)
F_z	Lift force (N)
g	Gravitational acceleration = 9.81 m s^{-2}
Kn	Knudsen number
l	Distance between spheres
m	Mass of the sphere
Ma	Mach number
p	Pressure (Pa)
r	radius of the sphere (m)
Re	Reynolds number
R_m	Specific gas constant = 287.058 m^2 s^{-2} K^{-1}
R_s	Radial distance of the middle shock
$\boldsymbol{T}$	Tension force of the wire (N)
Te	Temperature (K)
U	Flow speed (m s^{-1})
	Subscript
∞	Free-stream conditions
0	Stagnation conditions
1	First sphere (fixed)
2	Second sphere (moving)

Table 3. Nomenclature

References

Ahmad, N. & Fitri, E. 2021 Preliminary determination of footprint area of uncontrolled space debris: case study of Tiangong-1 space station. *Indones. J. Geogr.* **53** (2), 192–197.

Ailor, W., Hallman, W., Steckel, G. & Weaver, M. 2005 Analysis of reentered debris and implications for survivability modeling. In *4th European Conference on Space Debris*, vol. 587, p. 539. ESA.

Ailor, W.H. & Patera, R.P. 2007 Spacecraft re-entry strategies: meeting debris mitigation and ground safety requirements. *Proc. Inst. Mech. Engrs* **221** (6), 947–953.

Akhlaghi, H. & Roohi, E. 2021 Generalized description of the Knudsen layer thickness in rarefied gas flows. *Phys. Fluids* **33** (6), 061701.

Annaloro, J., Galera, S., Kärräng, P., Prigent, G., Lips, T. & Omaly, P. 2017 Comparison between two spacecraft-oriented tools: PAMPERO & SCARAB. *J. Space Safety Engng* **4** (1), 15–21.

AROESTY, J. 1962 Sphere drag in low density supersonic flow. *Tech. Rep.* HE-150-192. California University Berkley Institute of Engineering Research.

BAILEY, A.B. 1966 Sphere drag measurement in aeroballistics range at high velocities and low Reynolds numbers. *Tech. Rep.* AEDC-TR-66-59. ARO INC ARNOLD AFS TN.

BIRD, G.A. 1994 *Molecular Gas Dynamics and the Direct Simulation of Gas Flows*. Clarendon.

BOLDYREV, S.M., BOROVOY, V.Y., CHINILOV, A.Y., GUSEV, V.N., KRUTIY, S.N., STRUMINSKAYA, I.V., YAKOVLEVA, L.V., DÉLERY, J. & CHANETZ, B. 2001 A thorough experimental investigation of shock/shock interferences in high Mach number flows. *Aerosp. Sci. Technol.* **5** (3), 167–178.

BOROVOY, V.Y., CHINILOV, A.Y., GUSEV, V.N., STRUMINSKAYA, I.V., DÉLERY, J. & CHANETZ, B. 1997 Interference between a cylindrical bow shock and a plane oblique shock. *AIAA J.* **35** (11), 1721–1728.

CARDONA, V., JOUSSOT, R. & LAGO, V. 2021 Shock/shock interferences in a supersonic rarefied flow: experimental investigation. *Exp. Fluids* **62** (6), 1–14.

CARDONA, V. & LAGO, V. 2022 Aerodynamic forces of interacting spheres representative of space debris re-entry: experiments in a supersonic rarefied wind-tunnel. *Acta Astronaut.* **191**, 148–159.

CARLSON, A.B. & WILMOTH, R.G. 1992 Shock interference prediction using direct simulation Monte Carlo. *J. Spacecr. Rockets* **29** (6), 780–785.

CHAMBRE, P.A. & SCHAAF, S.A. 1961 Flow of rarefied gases. In *Flow of Rarefied Gases* (ed. C. duP. Donaldson). Princeton University Press.

COUMAR, S. & LAGO, V. 2017 Influence of Mach number and static pressure on plasma flow control of supersonic and rarefied flows around a sharp flat plate. *Exp. Fluids* **58** (6), 74.

DOGRA, V.K., MOSS, J.N., WILMOTH, R.G. & PRICE, J.M. 1994 Hypersonic rarefied flow past spheres including wake structure. *J. Spacecr. Rockets* **31** (5), 713–718.

EDNEY, B. 1968 Anomalous heat transfer and pressure distributions on blunt bodies at hypersonic speeds in the presence of an impinging shock. *Tech. Rep.* FFA-115. Flygtekniska Forsoksanstalten.

ESOC 2021 ESA's Annual Space Environment Report. *Tech. Rep.* GEN-DB-LOG-00288-OPS-SD. ESA.

FISHER, T.B. 2019 *Development of Advanced Techniques for Aerodynamic Assessment of Blunt Bodies in Hypersonic Flows*. University of Manchester.

FISHER, T., QUINN, M.K. & SMITH, K. 2018 Free-flight testing of hypersonic Edney shock interactions. In *2018 Aerodynamic Measurement Technology and Ground Testing Conference*, p. 4283.

FLORES-ABAD, A., MA, O., PHAM, K. & ULRICH, S. 2014 A review of space robotics technologies for on-orbit servicing. *Prog. Aerosp. Sci.* **68**, 1–26.

GLASS, C.E. 1999 Numerical simulation of low-density shock-wave interactions. *NASA Tech. Rep.* TM-1999-209358.

GOLUBEV, V.K. 2012 Computational visualization of aerodynamic interaction of simple objects in supersonic flows. In *15th International Symposium on Flow Visualization*.

GRASSO, F., PURPURA, C., CHANETZ, B. & DÉLERY, J. 2003 Type III and type IV shock/shock interferences: theoretical and experimental aspects. *Aerosp. Sci. Technol.* **7** (2), 93–106.

GUSEV, V.N. & EROFEEV, A.I. 2004 Oblique shock/bow shock interference in rarefied flow past a cylinder. *Fluid Dyn.* **39** (5), 827–835.

HOSSEIN, S.H., ACERNESE, M., CARDONA, T., CIALONE, G., CURIANÒ, F., MARIANI, L., MARINI, V., MARZIOLI, P., PARISI, L. & PIERGENTILI, F. 2020 Sapienza space debris observatory network (SSON): a high coverage infrastructure for space debris monitoring. *J. Space Safety Engng* **7** (1), 30–37.

KÄRRÄNG, P., LIPS, T. & SOARES, T. 2019 Demisability of critical spacecraft components during atmospheric re-entry. *J. Space Safety Engng* **6** (3), 181–187.

KEYES, J.W. & HAINS, F.D. 1973 Analytical and experimental studies of shock interference heating in hypersonic flows. *NASA Tech. Rep.* TN-D-7139.

KHATTA, A. & GOPALAN, J. 2018 Hypersonic shock tunnel studies of Edney type III and IV shock interactions. *Aerosp. Sci. Technol.* **72**, 335–352.

KOPPENWALLNER, G., FRITSCHE, B. & LIPS, T. 2001 Survivability and ground risk potential of screws and bolts of disintegrating spacecraft during uncontrolled re-entry. In *3rd European Conference on Space Debris*, pp. 533–539. ESA.

KOPPENWALLNER, G., FRITSCHE, B., LIPS, T. & HEINER, K. 2005 SCARAB – a multi-disciplinary code for destruction analysis of space-craft during re-entry. In *Fifth European Symposium on Aerothermodynamics for Space Vehicles* (ed. D. Danesy), p. 281.

KOVACS, L., PASSAGGIA, P.-Y., MAZELLIER, N. & LAGO, V. 2022 Detection method for shock-waves in viscous flows. *Exp. Fluids* **63** (1), 1–16.

LAURENCE, S.J. & DEITERDING, R. 2011 Shock-wave surfing. *J. Fluid Mech.* **676**, 396–431.

LAURENCE, S.J., DEITERDING, R. & HORNUNG, G. 2007 Proximal bodies in hypersonic flow. *J. Fluid Mech.* **590**, 209–237.

LAURENCE, S.J., PARZIALE, N.J. & DEITERDING, R. 2012 Dynamical separation of spherical bodies in supersonic flow. *J. Fluid Mech.* **713**, 159–182.

LEISER, D., LÖHLE, S., ZANDER, F., BUTTSWORTH, D.R., CHOUDHURY, R. & FASOULAS, S. 2022 Analysis of reentry and break-up forces from impulse facility experiments and numerical rebuilding. *J. Spacecr. Rockets* **59** (4), 1275–1288.

LIPS, T. 2003 Re-entry analysis of Terrasar-X with SCARAB. In *54th International Astronautical Congress of the International Astronautical Federation, the International Academy of Astronautics, and the International Institute of Space Law*, pp. IAA–5.

LIPS, T. 2013 Equivalent re-entry breakup altitude and fragment list. In *6th European Conference on Space Debris*, p. 54. ESA.

LIPS, T. & FRITSCHE, B. 2005 A comparison of commonly used re-entry analysis tools. *Acta Astronaut.* **57** (2–8), 312–323.

LIPS, T., FRITSCHE, B., KOPPENWALLNER, G. & KLINKRAD, H. 2004 Spacecraft destruction during re-entry – latest results and development of the SCARAB software system. *Adv. Space Res.* **34** (5), 1055–1060.

LU, H., YUE, L., XIAO, Y. & ZHANG, X. 2013 Interaction of isentropic compression waves with a bow shock. *AIAA J.* **51** (10), 2474–2484.

MACROSSAN, M.N. 2007 Scaling parameters for hypersonic flow: correlation of sphere drag data. In *25th International Symposium on Rarefied Gas Dynamics*, pp. 759–764.

MARWEGE, A., WILLEMS, S., GÜLHAN, A., AFTOSMIS, M.J. & STERN, E.C. 2018 Superposition method for force estimations on bodies in supersonic and hypersonic flows. *J. Spacecr. Rockets* **55** (5), 1166–1180.

MORE, A. & MURUGAN, S. 2021 Dynamics of morphing robotic arm with space debris capture. In *8th European Conference on Space Debris*. ESA Space Debris Office.

MOSS, J.N., POT, T., CHANETZ, B. & LEFEBVRE, M. 1999 DSMC simulation of shock/shock interactions: emphasis on type IV interactions. In *22nd International Symposium on Shock Waves, London*.

MUTHOO, S.K. & BRUNDIN, C.L. 1974 Near wake flow field measurements behind spheres in low Reynolds number hypersonic flow. In *9th International Symposium on Rarefied Gas Dynamics, Göttingen, July 1974* (ed. M. Becker). DFVLR.

NOUBEL, H. & LAGO, V. 2021 Experimental analysis of waverider lift-to-drag ratio measurements in rarefied and supersonic regime. In *Hypersonic Vehicles – Applications, Recent Advances, and Perspectives* (ed. G. Pezzella & A. Viviani). IntechOpen.

OSTROM, C. & SANCHEZ, C. 2018 ORSAT modelling and assessment. In *4th International Workshop on Space Debris Re-Entry*. NASA.

PAOLI, R. 2018 Numerical simulations of shock–shock interactions. *Open J. Fluid Dyn.* **8** (4), 392–403.

PARK, C. & BROWN, J.D. 2012 Fragmentation and spreading of a meteor-like object. *Astron. J.* **144** (6), 184.

PARK, S.H., LABOULAIS, J.N., LEYLAND, P. & MISCHLER, S. 2020 Re-entry survival analysis and ground risk assessment of space debris considering by-products generation. *Acta Astronaut.* **179**, 604–618.

PARK, S.H. & PARK, G. 2017 Reentry trajectory and survivability estimation of small space debris with catalytic recombination. *Adv. Space Res.* **60** (5), 893–906.

PENG, J., LUO, C.T., HAN, Z.J., HU, Z.M., HAN, G.L. & JIANG, Z.L. 2020 Parameter-correlation study on shock–shock interaction using a machine learning method. *Aerosp. Sci. Technol.* **107**, 106247.

POT, T., CHANETZ, B., LEFEBVRE, M. & BOUCHARDY, P. 1999 Fundamental study of shock/shock interference in low density flow: flowfield measurements by DLCARS. In *RGD: rarefied gas dynamics (Marseille, 26–31 July 1998)*, pp. 545–552.

PREVEREAUD, Y., VÉRANT, J.L., MOSCHETTA, J.M., SOURGEN, F. & BLANCHARD, M. 2012 Debris aerodynamic interactions during uncontrolled atmospheric reentry. In *AIAA Atmospheric Flight Mechanics Conference*, p. 4582.

REEVES, B.L. & LEES, L. 1965 Theory of laminar near wake of blunt bodies in hypersonic flow. *AIAA J.* **3** (11), 2061–2074.

REGISTER, P.J., AFTOSMIS, M.J., STERN, E.C., BROCK, J.M., SELTNER, P.M., WILLEMS, S., GUELHAN, A. & MATHIAS, D.L. 2020 Interactions between asteroid fragments during atmospheric entry. *Icarus* **337**, 113468.

REMBAUT, N., JOUSSOT, R. & LAGO, V. 2020 Aerodynamical behavior of spherical debris in the supersonic and rarefied wind tunnel MARHy. *J. Space Safety Engng* **7** (3), 411–419.

REYHANOGLU, M. & ALVARADO, J. 2013 Estimation of debris dispersion due to a space vehicle breakup during reentry. *Acta Astronaut.* **86**, 211–218.

RIABOV, V.V. & BOTIN, A.V. 1999 Shock interference in hypersonic rarefied-gas flows near a cylinder. In *17th Applied Aerodynamics Conference*, p. 3207.

SANDERSON, S. 1995 Shock wave interaction in hypervelocity flow. PhD thesis, California Institute of Technology.

VASHCHENKOV, P., KASHKOVSKY, A. & IVANOV, M. 2003 Aerodynamics of fragment in spacecraft wake. In *Rarefied Gas Dynamics: 23rd International Symposium* (ed. A.D. Ketsdever & E.P. Muntz), pp. 226–233. American Institute of Physics.

WEGENER, P.P. & ASHKENAS, H. 1961 Wind tunnel measurements of sphere drag at supersonic speeds and low Reynolds numbers. *J. Fluid Mech.* **10** (4), 550–560.

WHALEN, T.J. & LAURENCE, S.J. 2021 Experiments on the separation of sphere clusters in hypersonic flow. *Exp. Fluids* **62** (4), 1–19.

WHITE, C. & KONTIS, K. 2018 The effect of increasing rarefaction on the Edney type IV shock interaction problem. In *Shock Wave Interactions: Selected Articles from the 22nd International Shock Interaction Symposium, University of Glasgow, UK, 4–8 July 2016*, pp. 299–311. Springer.

WINDISCH, C., REINARTZ, B.U. & MÜLLER, S. 2016 Investigation of unsteady Edney type IV and VII shock–shock interactions. *AIAA J.* **54** (6), 1846–1861.

WUEST, W. 1974 Simulation of high altitude flight in wind-tunnels and correlation of free-flight and wind tunnel data. In *9th Congress of the International Council of the Aeronautical Sciences*, pp. 357–368.

ZHU, C., LIANG, S.C. & FAN, L.S. 1994 Particle wake effects on the drag force of an interactive particle. *Intl J. Multiphase Flow* **20** (1), 117–129.

ZUPPARDI, G. & PATERNA, D. 2015 Influence of partial accommodation coefficients on the aerodynamic parameters of an airfoil in hypersonic, rarefied flow. *Adv. Aircraft Spacecr. Sci.* **2** (4), 427.